

Towards a Complete Census of AGNs in Nearby Galaxies: A Large Population of Optically Unidentified AGNs

A.D. Goulding^{*} & D.M. Alexander

Department of Physics, Durham University, South Road, Durham.

Released 2009 Xxxxx XX

ABSTRACT

Using *Spitzer*-IRS spectroscopy, we investigate the ubiquity of Active Galactic Nuclei (AGN) in a complete (≈ 94 percent), volume-limited sample of the most bolometrically-luminous galaxies ($L_{\text{IR}, 8-1000 \mu\text{m}} \gtrsim (0.3-20) \times 10^{10} L_{\odot}$) to $D < 15$ Mpc. Our analyses are based on the detection of the high-excitation emission line [NeV] $\lambda 14.32 \mu\text{m}$ (97.1 eV) to unambiguously identify AGN activity. We find that 17 of the 64 IR-bright galaxies in our sample host AGN activity ($\approx 27_{-6}^{+8}$ percent), $\gtrsim 50$ percent of which are not identified as AGNs using optical spectroscopy. The large AGN fraction indicates a tighter connection between AGN activity and IR luminosity for galaxies in the local Universe than previously found, potentially indicating a close association between AGN activity and star formation. The optically unidentified AGNs span a wide range of galaxy type (S0–Ir) and are typically starburst-dominated systems hosting modest-luminosity AGN activity ($L_{[\text{NeV}]} \approx 10^{37-10^{39}} \text{erg s}^{-1}$). The non-identification of optical AGN signatures in the majority of these galaxies appears to be due to extinction towards the AGN, rather than intrinsically low-luminosity AGN activity; however, we note that the AGN optical signatures are diluted in some galaxies due to strong star-formation activity. Examination of optical images shows that the optically unidentified AGNs with evidence for extinction are hosted in either highly inclined galaxies or galaxies with dust lanes, indicating that obscuration of the AGN is not necessarily due to an obscuring torus. We therefore conclude that optical spectroscopic surveys miss approximately half of the AGN population simply due to extinction through the host galaxy.

Key words: galaxies: active – galaxies: evolution – galaxies: nuclei – infrared: galaxies

1 INTRODUCTION

The seminal discovery that all massive galaxies in the local Universe harbour super-massive black holes (SMBHs; $M_{\text{BH}} > 10^6 M_{\odot}$) implies that all massive galaxies have hosted Active Galactic Nuclei (AGN) at some time during the last ≈ 13 Gyrs (e.g., Kormendy & Richstone 1995; Magorrian et al. 1998; Gebhardt et al. 2000). Sensitive blank-field surveys have traced the evolution of luminous AGN activity out to $z \approx 5-6$, providing a window on the growth of SMBHs across $\approx 95\%$ of cosmic time (e.g., Ueda et al. 2003; Croom et al. 2004; Fan et al. 2004; Hasinger et al. 2005; Richards et al. 2006). However, these blank-field surveys typically lack the volume and sensitivity to provide a complete census of AGN activity in the local Universe. Such a census is required to (1) provide a baseline with which to interpret the results obtained for distant AGNs from blank-field surveys, and (2) provide definitive

constraints on the growth of SMBHs in the local Universe (e.g., the growth rates of SMBHs; the relative amount of obscured and unobscured SMBH growth; the galaxies and environments where SMBHs are growing).

Arguably, the most complete census of AGN activity in the local Universe is the optical spectroscopic survey of Ho et al. (1997a,b; hereafter Ho97). Ho97 classified nearly all galaxies with $B_T \leq 12.5$ mag in the Northern hemisphere and identified AGNs on the basis of the relative strength of forbidden and permitted emission lines (e.g., Baldwin et al. 1981; Veilleux & Osterbrock 1987; Kewley et al. 2001); objects with a broad permitted line component ($\text{FWHM} > 1000 \text{ km s}^{-1}$) were also classified as AGNs. Using this classification scheme, Ho97 found that $\approx 10\%$ of galaxies unambiguously host AGN activity (i.e., optically classified as Seyfert galaxies). These AGNs were found to predominantly reside in moderately massive bulge-dominated galaxies (Hubble type E–Sbc). However, since the source selection and classification were performed at optical wavelengths, the Ho97 studies were insensitive to the identification of the

^{*} E-mail:- andrew.goulding@durham.ac.uk

most heavily dust-obscured AGNs. For example, the nearby Scd galaxy, NGC 4945 is classified as a starburst galaxy at optical wavelengths and only reveals the presence of AGN activity using mid-IR spectroscopy (Spoon et al. 2000) and X-ray observations (Iwasawa et al. 1993). Various studies have suggested that NGC 4945 is unlikely to be a particularly unusual AGN (e.g., Lutz et al. 2003; Maiolino et al. 2003), indicating that there may be many more optically unidentified AGNs in the local Universe.

X-ray observations have revealed potential AGNs in many galaxies in the Ho97 sample lacking optical AGN signatures (e.g., Ho et al. 2001; Desroches & Ho 2009). However, there is often ambiguity over whether an AGN is producing the X-ray emission in these galaxies (e.g., there can be significant contamination from X-ray binaries). Furthermore, the X-ray emission from Compton-thick AGNs ($N_{\text{H}} > 1.5 \times 10^{24} \text{ cm}^{-2}$) can be extremely weak, making it challenging to identify the most heavily obscured AGNs using X-ray data alone (i.e., the $< 10 \text{ keV}$ emission can be a factor ≈ 30 – 1000 times weaker than the intrinsic emission; e.g., Risaliti et al. 1999; Matt et al. 2000). By comparison, due to the extreme conditions required to produce the high ionization emission line [NeV] $\lambda 14.32, 24.32 \text{ }\mu\text{m}$ (97.1 eV), mid-IR spectroscopy provides an unambiguous indicator of AGN activity in nearby galaxies (e.g., Weedman et al. 2005; Armus et al. 2006).¹ The relative optical depth at mid-IR wavelengths is also considerably lower than at optical wavelengths ($A_{\lambda 14.3 \text{ }\mu\text{m}}/A_{\text{V}} \approx 50$; Li & Draine 2001). Even heavily Compton-thick AGNs that are weak at X-ray energies can be identified using mid-IR spectroscopy (e.g., the well-studied NGC 1068 with $N_{\text{H}} > 10^{25} \text{ cm}^{-2}$ has bright [NeV] $\lambda 14.32 \text{ }\mu\text{m}$ emission; Sturm et al. 2002). Thus, the identification of high-ionization [NeV] $\lambda 14.32, 24.32 \text{ }\mu\text{m}$ provides a relatively optically thin means by which to probe the central engine of nearby AGNs. On the basis of the identification of [NeV] emission in a heterogeneous sample of late-type spiral galaxies within the local Universe, Satyapal et al. (2008; hereafter, S08) have suggested that a large number of Sc–Sm galaxies host optically unidentified AGN activity.

Local mid-IR surveys (e.g., Sturm et al. 2002; the *Spitzer* Infrared Nearby Galaxy Survey [SINGS] Legacy Project [Dale et al. 2006; hereafter D06] and S08) have shown the advantages of using mid-IR spectroscopy as an AGN diagnostic. However, none of these studies have used this diagnostic to provide a complete unambiguous census of AGN activity within the local Universe. Here we use sensitive high-resolution *Spitzer*-IRS spectroscopy to identify AGNs within a complete (≈ 94 percent) volume-limited survey of the most bolometrically luminous galaxies ($L_{\text{IR}} > 3 \times 10^9 L_{\odot}$) to a distance of $D < 15 \text{ Mpc}$.² By selecting galaxies at IR wavelengths, our sample will comprise the most active galaxies in the local Universe and will also include the most dust-obscured systems. We use these data to unambiguously identify AGNs using the high-ionization [NeV] $\lambda 14.32 \text{ }\mu\text{m}$ emission line to produce the most sensitive

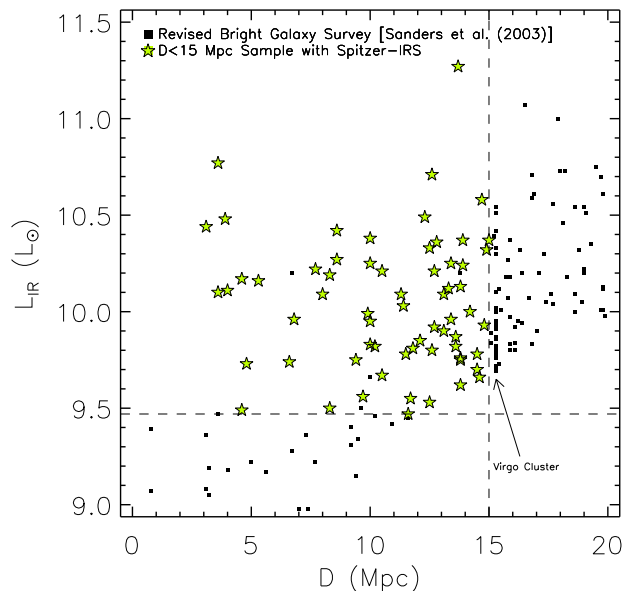


Figure 1. Logarithm of IR luminosity versus luminosity distance for all objects in the RBGS (Sanders et al. 2003; squares). The 64 IR-bright galaxies ($L_{\text{IR}} \approx 3 \times 10^9 L_{\odot}$) to $D < 15 \text{ Mpc}$ with high-resolution *Spitzer*-IRS spectroscopy are explored here (stars).

census of AGN activity in the local Universe to date. In §2 we outline the construction and data reduction analysis of the sample assembled from the *IRAS* Revised Bright Galaxy Survey of Sanders et al. (2003; RBGS). In §3 we determine the fraction of local galaxies hosting AGN activity, explore their properties, and compare the results to the previous optical survey of Ho97 to address the key question: Why are a large number of AGNs unidentified at optical wavelengths? In §4 we present our conclusions.

2 THE SAMPLE AND DATA REDUCTION

2.1 Sample Selection

Using *IRAS*, the RBGS (Sanders et al. 2003) has provided an accurate census of all IR-bright galaxies ($|b| > 5^\circ$, $f_{60\mu\text{m}} > 5.24 \text{ Jy}$) in the local Universe. The aim of our study is to identify AGN activity in the most bolometrically luminous galaxies ($L_{\text{IR}} > 3 \times 10^9 L_{\odot}$) out to $D < 15 \text{ Mpc}$.³ The distance constraint of 15 Mpc was placed so as to not include the Virgo cluster at 16 Mpc (i.e., to be representative of field-galaxy populations). The IR luminosity threshold was chosen to be well matched to the flux limit of the RBGS (see Fig. 1) and ensures that we do not include low-luminosity dwarf galaxies and relatively inactive galaxies. In the RBGS there are 68 *IRAS* detected galaxies to a

¹ We note that [OIV] $\lambda 25.9 \text{ }\mu\text{m}$ (54.9 eV) is also often used for AGN identification, although energetic starbursts can also produce luminous [OIV] emission; see §3.4.

² L_{IR} corresponds to the 8–1000 μm luminosity, as defined by Sanders & Mirabel (1996).

³ Distances have been calculated using the cosmic attractor model of Mould et al. (2000), which adjusts heliocentric redshifts to the centroid of the local group, taking into account the gravitational attraction towards the Virgo cluster, the Great Attractor, and the Shapley supercluster.

Table 1. Catalogue of sources and derived quantities.

Common Name (1)	RA (2)	DEC (3)	Dist (Mpc) (4)	SH (kpc) (5)	LH (kpc) (6)	Morph Class (7)	L_{IR} (L_{\odot}) (8)	Spectral Class (9)	$\frac{H_{\alpha}}{H_{\beta}}$ (10)	$\frac{[\text{OIII}]}{H_{\beta}}$ (11)	$\frac{[\text{SII}]}{H_{\alpha}}$ (12)	$\frac{[\text{NII}]}{H_{\alpha}}$ (13)	$10^{15} f_{[\text{OIII}]}$ ($\text{erg cm}^{-2} \text{s}^{-1}$) (14)	Ref. (15)
ESO 121-G006	06h07m29.5s	-61d48m28s	14.5	0.33×0.79	0.78×1.57	Sc	9.70	-	-	-	-	-	-	-
ESO 209-G009	07h58m14.9s	-49d51m09s	11.8	0.27×0.65	0.64×1.28	Scd	9.81	-	-	-	-	-	-	-
ESO 265-G007	11h07m48.8s	-46d31m38s	11.7	0.27×0.64	0.63×1.26	Scd	9.55	-	-	-	-	-	-	-
IC 2056	04h16m24.2s	-60d12m26s	13.8	0.31×0.76	0.74×1.49	Sbc	9.62	-	-	-	-	-	-	-
IC 342	03h46m49.4s	+68d05m49s	4.6	0.10×0.25	0.25×0.50	Scd	10.17	HII	3.27	0.10	0.22	0.45	0.90	1
IIZW40	05h55m42.0s	+03d23m30s	11.6	0.26×0.64	0.62×1.25	Sbc	9.47	HII	2.89	6.31	0.05	0.04	22574.40	6
M 82	09h55m53.1s	+69d40m41s	3.6	0.08×0.20	0.19×0.40	Ir	10.77	HII	21.93	0.36	0.18	0.56	66.15	1
NGC 0253	00h47m33.1s	-25d17m15s	3.1	0.07×0.17	0.17×0.34	Sc	10.44	HII	0.47	0.36	0.34	0.72	27.06	2
NGC 0278	00h52m04.3s	+47d33m01s	11.4	0.26×0.62	0.61×1.23	Sab	10.03	HII	3.84	0.24	0.28	0.50	1.89	1
NGC 0613	01h34m17.8s	-29d25m10s	15.0	0.34×0.82	0.81×1.62	Sbc	10.37	HII	6.80	0.48	0.35	0.59	17.22	4
NGC 0628	01h36m41.2s	+15d47m29s	10.0	0.23×0.55	0.54×1.08	Sc	9.95	HII	-	0.61	0.13	0.41	7.62	8
NGC 0660	01h43m02.1s	+13d38m45s	12.3	0.28×0.67	0.66×1.33	Sa	10.49	L	13.65	2.19	0.43	0.85	7.72	1
NGC 0891	02h22m33.5s	+42d21m18s	8.6	0.20×0.47	0.46×0.93	Sab	10.27	HII	12.37	1.00	0.30	0.29	0.18	1
NGC 1055	02h41m44.3s	+00d26m36s	11.3	0.26×0.62	0.61×1.22	Sb	10.09	L	-	-	0.41	0.66	-	1
NGC 1068	02h42m41.4s	+00d00m45s	13.7	0.31×0.75	0.74×1.48	Sb	11.27	S2 (1.8)	5.29	12.82	0.24	0.76	38235.10	1
NGC 1448	03h44m32.1s	-44d38m41s	11.5	0.26×0.63	0.62×1.24	Scd	9.78	HII	> 1.67	-	1.60	0.60	< 0.60	4
NGC 1559	04h17m37.4s	-62d46m59s	12.7	0.29×0.70	0.68×1.37	Scd	10.21	HII	> 3.14	> 1.00	0.82	-	0.70	4
NGC 1569	04h30m49.5s	+64d51m01s	4.6	0.10×0.25	0.25×0.50	Ir	9.49	HII	3.74	5.48	0.03	0.04	10.14	1
NGC 1792	05h05m13.7s	-37d58m46s	12.5	0.28×0.68	0.67×1.35	Sbc	10.33	HII	-	0.16	0.21	0.54	0.30	4
NGC 1808	05h07m42.3s	-37d30m48s	12.6	0.29×0.69	0.68×1.36	Sa	10.71	HII	2.95	0.16	0.21	0.54	16.31	2
NGC 2681	08h53m33.6s	+51d18m46s	12.5	0.28×0.68	0.67×1.35	Sa	9.53	L	4.77	1.74	0.76	2.34	12.66	1
NGC 2903	09h32m10.5s	+21d30m05s	8.3	0.19×0.45	0.45×0.90	Sbc	10.19	HII	4.42	0.03	0.19	0.34	2.66	1
NGC 3059	09h50m08.1s	-73d55m24s	14.2	0.32×0.78	0.76×1.54	Sbc	10.00	-	-	-	-	-	-	-
NGC 3175	10h14m42.9s	-28d52m25s	13.4	0.31×0.73	0.72×1.45	Sb	9.96	HII	-	-	-	-	-	-
NGC 3184	10h18m12.1s	+41d25m53s	12.6	0.29×0.69	0.68×1.36	Scd	9.80	HII	4.42	0.13	0.20	0.33	1.07	1
NGC 3198	10h19m55.6s	+45d32m54s	13.8	0.31×0.76	0.74×1.49	Sc	9.75	HII	6.44	0.23	0.32	0.42	0.41	1
NGC 3351	10h43m58.1s	+11d42m10s	10.0	0.23×0.55	0.54×1.08	Sb	9.83	HII	4.38	0.27	0.24	0.46	2.19	1
NGC 3368	10h46m45.6s	+11d49m13s	10.5	0.24×0.58	0.57×1.14	Sab	9.67	L	7.46	1.82	0.98	1.12	3.24	1
NGC 3511	11h03m24.2s	-23d05m15s	13.6	0.31×0.75	0.73×1.47	Sc	9.82	HII	12.30	0.28	0.27	0.44	-	7
NGC 3521	11h05m49.2s	+00d02m15s	6.8	0.15×0.37	0.37×0.74	Sbc	9.96	L	3.71	1.00	0.87	0.65	7.39	1
NGC 3556	11h11m31.5s	+55d40m23s	13.9	0.32×0.76	0.75×1.50	Scd	10.37	HII	7.29	0.26	0.29	0.32	1.81	1
NGC 3621	11h18m16.7s	-32d48m47s	6.6	0.15×0.36	0.36×0.71	Sd	9.74	S2	3.42	8.61	0.21	1.46	2.24	9
NGC 3627	11h20m15.3s	+12d59m32s	10.0	0.23×0.55	0.54×1.08	Sb	10.38	L	5.92	2.90	0.76	1.45	12.95	1
NGC 3628	11h20m17.4s	+13d35m19s	10.0	0.23×0.55	0.54×1.08	Sb	10.25	L	4.72	1.78	0.78	0.95	0.23	1
NGC 3675	11h26m09.0s	+43d35m04s	12.7	0.29×0.70	0.68×1.37	Sab	9.92	L	3.20	1.29	0.68	1.48	3.21	1
NGC 3726	11h33m19.9s	+47d01m49s	14.5	0.33×0.79	0.78×1.57	Sc	9.78	HII	3.44	0.14	0.22	0.31	2.52	1
NGC 3938	11h52m49.2s	+44d07m14s	14.8	0.34×0.81	0.80×1.60	Sc	9.93	HII	2.82	1.78	0.83	0.52	1.19	1
NGC 3949	11h53m42.0s	+47d51m31s	13.6	0.31×0.75	0.73×1.47	Sbc	9.87	HII	3.51	0.22	0.44	0.40	1.24	1
NGC 4013	11h58m31.5s	+43d56m54s	13.8	0.31×0.76	0.74×1.49	Sb	9.76	L	2.05	0.71	0.83	1.12	1.01	1
NGC 4051	12h03m09.8s	+44d31m50s	13.1	0.30×0.72	0.70×1.42	Sbc	9.90	S2 (1.5)	3.30	4.47	0.36	0.65	726.25	1

Table 1 – *continued*

Common Name (1)	RA (2)	DEC (3)	Dist (Mpc) (4)	SH (kpc) (5)	LH (kpc) (6)	Morph Class (7)	L_{IR} (L_{\odot}) (8)	Spectral Class (9)	$\frac{H_{\alpha}}{H_{\beta}}$ (10)	$\frac{[\text{OIII}]}{H_{\beta}}$ (11)	$\frac{[\text{SII}]}{H_{\alpha}}$ (12)	$\frac{[\text{NII}]}{H_{\alpha}}$ (13)	$10^{15} f_{[\text{OIII}]}$ ($\text{erg cm}^{-2} \text{s}^{-1}$) (14)	Ref. (15)
NGC 4085	12h05m23.3s	+50d21m08s	14.6	0.33×0.80	0.79×1.58	Sc	9.66	HII	4.71	0.63	0.19	0.32	172.71	6
NGC 4088	12h05m35.1s	+50d32m24s	13.4	0.31×0.73	0.72×1.45	Sbc	10.25	HII	7.04	0.21	0.18	0.32	1.40	1
NGC 4157	12h11m04.2s	+50d29m04s	13.3	0.30×0.73	0.72×1.44	Sab	10.12	HII	10.69	0.22	0.24	0.34	0.43	1
NGC 4490	12h30m34.9s	+41d38m47s	10.5	0.24×0.58	0.57×1.14	Sd	10.21	L	6.39	2.57	0.71	0.25	1.83	1
NGC 4536	12h34m28.5s	+02d11m08s	14.9	0.34×0.82	0.80×1.61	Sbc	10.32	HII	5.23	0.33	0.36	0.47	5.42	1
NGC 4559	12h35m57.0s	+27d57m37s	9.7	0.22×0.53	0.52×1.05	Scd	9.56	HII	3.59	0.35	0.40	0.42	0.90	1
NGC 4631	12h42m07.1s	+32d32m33s	7.7	0.18×0.42	0.41×0.83	Sd	10.22	HII	3.07	1.51	0.23	0.24	1.85	1
NGC 4666	12h45m07.7s	+00d27m41s	12.8	0.29×0.70	0.69×1.38	Sc	10.36	L	5.13	1.20	0.60	1.29	558.28	3
NGC 4736	12h50m52.9s	+41d07m15s	4.8	0.11×0.26	0.26×0.52	Sab	9.73	L	3.14	1.47	1.39	2.15	9.59	1
NGC 4818	12h56m50.0s	-08d31m38s	9.4	0.21×0.51	0.51×1.02	Sab	9.75	HII	2.95	0.15	0.18	0.63	-	2
NGC 4945	13h05m27.6s	-49d28m09s	3.9	0.09×0.21	0.21×0.42	Scd	10.48	HII	1.20	< 0.90	0.15	0.30	< 1.00	5
NGC 5033	13h13m27.2s	+36d35m40s	13.8	0.31×0.76	0.74×1.49	Sc	10.13	S2 (1.9)	4.48	4.68	1.07	2.34	96.28	1
NGC 5055	13h15m49.5s	+42d01m39s	8.0	0.18×0.44	0.43×0.86	Sbc	10.09	L	5.42	1.86	0.74	1.48	3.61	1
NGC 5128	13h25m27.6s	-43d01m12s	4.0	0.09×0.22	0.22×0.43	S0	10.11	HII	5.50	0.55	0.28	0.45	12.06	4
NGC 5194	13h29m53.5s	+47d11m42s	8.6	0.20×0.47	0.46×0.93	Sbc	10.42	S2	8.44	8.91	0.85	2.88	90.87	1
NGC 5195	13h30m00.0s	+47d16m00s	8.3	0.19×0.45	0.45×0.90	Irr	9.50	L	1.90	1.22	2.00	5.37	6.76	1
NGC 5236	13h36m58.8s	-29d51m46s	3.6	0.08×0.20	0.19×0.39	Sc	10.10	HII	6.05	0.29	0.21	1.33	35.36	4
NGC 5643	14h32m41.1s	-44d10m30s	13.9	0.32×0.76	0.75×1.50	Sc	10.24	S2	7.80	10.67	0.71	1.15	607.36	4
NGC 5907	15h15m58.9s	+56d18m36s	12.1	0.28×0.66	0.65×1.31	Sc	9.85	HII	11.81	1.07	0.34	0.60	0.44	1
NGC 6300	17h17m00.3s	-62d49m13s	13.1	0.30×0.72	0.70×1.42	Sb	10.09	S2	7.44	15.14	0.14	0.95	38.69	4
NGC 6744	19h09m45.9s	-63d51m27s	9.9	0.23×0.54	0.53×1.07	Sbc	9.99	L	0.90	1.30	2.44	-	6.75	4
NGC 6946	20h34m52.6s	+60d09m12s	5.3	0.12×0.29	0.29×0.57	Scd	10.16	HII	9.03	0.38	0.32	0.64	3.17	1
NGC 7331	22h37m04.6s	+34d24m56s	14.7	0.33×0.81	0.79×1.59	Sb	10.58	L	3.92	2.79	0.55	1.44	7.77	1
UGCA 127	06h20m56.9s	-08d29m42s	10.2	0.23×0.56	0.55×1.10	Scd	9.82	-	-	-	-	-	-	-

NOTES: (1) Common galaxy name. (2–3) *2MASS* near-IR position of galactic nucleus. (4) Luminosity distance to source in Mpc from the RBGS (Sanders et al. 2003). (5–6) Projected spectral apertures (SH and LH respectively) in kiloparsecs. (7) Morphological classification from RC3 (de Vaucouleurs et al. 1991). (8) Logarithm of IR luminosity (8–1000 μm) from RBGS. (9) Optical spectral class from BPT diagnostics (S2: Seyfert 2; broad-line sub-class in parentheses, HII: Star-forming galaxy, and L: LINER). (10–13) Optical emission line ratios. (14) Observed [OIII] flux in units of $10^{-15} \text{ erg cm}^{-2} \text{ s}^{-1}$. (15) References for published optical data.

REFERENCES: (1) Ho et al. (1997a); (2) Kewley et al. (2001); (3) Veilleux et al. (1995); (4) Veron-Cetty et al. (1986); (5) Moorwood et al. (1996); (6) Moustakas & Kennicutt (2006); (7) Kirhakos & Steiner (1990); (8) Ganda et al. (2006); (9) Barth et al. (2009).

Table 2. $D < 15$ Mpc IR-bright galaxies not included in sample

Common Name (1)	Morph Class (2)	Dist (Mpc) (3)	L_{IR} (L_{\odot}) (4)	Spectral Class (5)	<i>Spitzer</i> -IRS Spec? (6)	$L_{[\text{OIV}]}$ (erg s^{-1}) (7)
NGC 3486	Sc	9.2	9.31	Sy2	1	38.52
NGC 4565	Sb	10.0	9.66	Sy2	2	38.40
NGC 5248	Sbc	13.8	10.20	HII	3	-
NGC 5457	Scd	6.7	10.20	HII	2	-

NOTES: (1) Common galaxy name. (2) Morphological classification from RC3. (3) Luminosity distance in Mpc from RBGS. (4) Logarithm of IR luminosity (8–1000 μm) from RBGS. (5) Optical spectral class from Ho97 using BPT diagnostics; see Table 1. (6) Status of *Spitzer*-IRS data: 1. High-resolution observations are publicly available but signal-to-noise is not sufficient for analysis; 2. High-resolution observations available only for extranuclear regions; 3. No high-resolution observations available. (7) Logarithm of [OIV] $\lambda 25.89$ μm luminosity from low-resolution ($R \sim 100$) *Spitzer*-IRS spectroscopy in units of erg s^{-1} (Diamond-Stanic et al. 2009).

distance of $D < 15$ Mpc with $L_{\text{IR}} > 3 \times 10^9 L_{\odot}$, 64 of which have *Spitzer*-IRS high-resolution spectroscopy publicly available (i.e., ≈ 94 percent complete): P3124 (28 objects; PI: D.M. Alexander), P159 (18 objects; PI: R. Kennicutt [SINGS]), P14 (11 objects; PI: J.R. Houck), P59 (4 objects; PI: G. Rieke) and P86 (3 objects; PI: M. Werner).

In Fig. 1 we plot IR luminosity versus luminosity distance for the RBGS and highlight the 64 galaxies with *Spitzer*-IRS observations in our $D < 15$ Mpc sample. The basic properties from the RBGS for the sources are combined with published optical data and listed in Table 1. The objects are all late-type galaxies (Hubble classification of S0 or later), which is unsurprising since early-type galaxies are typically IR faint and undetected by *IRAS* (e.g., Knapp et al. 1989). The four galaxies that match our selection criteria but lack sufficient high-resolution *Spitzer*-IRS observations of the central regions are shown in Table 2. Specifically, NGC 3486 has Short-High (SH) and Long-High (LH) observations but the data are noisy and no statistically useful information can be extracted; NGC 4565 and NGC 5457 have only high-resolution observations of extranuclear regions; NGC 5248 has no high-resolution observations. NGC 5248 and NGC 5457 are optically classified as star-forming HII galaxies while NGC 3486 and NGC 4565 are optically classified as Seyfert galaxies (Ho97). Both NGC 3486 and NGC 4565 have published [OIV] $\lambda 25.89$ μm fluxes from low-resolution ($R \sim 100$) *Spitzer*-IRS spectroscopy in Diamond-Stanic et al. (2009); the derived [OIV] $\lambda 25.89$ μm luminosities suggest that the AGNs are contributing < 5 percent to the total bolometric luminosity of the galaxy.

2.2 Data Reduction

Each of the galaxies in our $D < 15$ Mpc sample were observed using both the SH ($4.7'' \times 11.3''$, $\lambda \sim 9.9\text{--}19.6$ μm) and LH ($11.1'' \times 22.3''$, $\lambda \sim 18.7\text{--}37.2$ μm) resolution spectrographs onboard the NASA *Spitzer* Space Telescope (Houck et al. 2004; Werner et al. 2004). The spectral resolution is $R \sim 600$ for both SH and LH modules. The raw

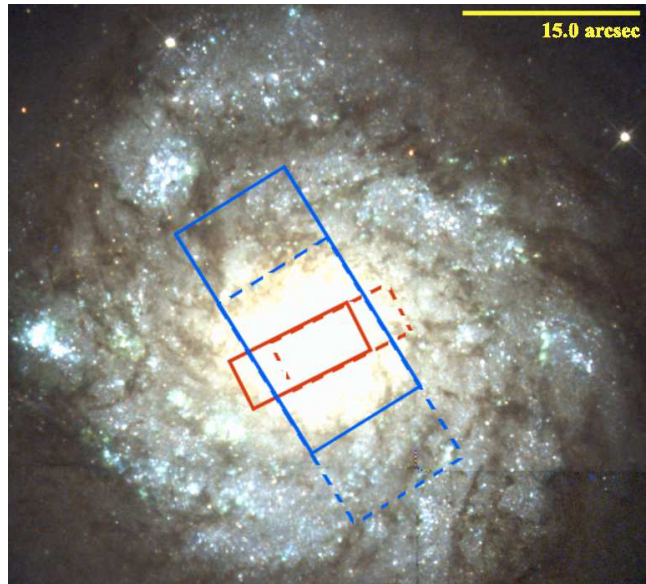


Figure 2. *Hubble Space Telescope* (HST) WFPC2 (3-colour) optical image of the circumnuclear region of a typical galaxy in the $D < 15$ Mpc sample, with *Spitzer*-IRS SH ($4.7'' \times 11.3''$, $\lambda \sim 9.9\text{--}19.6$ μm) and LH ($11.1'' \times 22.3''$, $\lambda \sim 18.7\text{--}37.2$ μm) apertures overlaid in the two nod positions (staring-mode observations). The object shown is the Sbc galaxy, NGC 0278 at $D \approx 11.4$ Mpc with $L_{\text{IR}} \approx 1.1 \times 10^{10} L_{\odot}$. Linear size-scales of apertures are $\approx 0.26 \times 0.63$ kpc (SH) and $\approx 0.61 \times 1.23$ kpc (LH). In highly resolved sources such as NGC 0278 the two nod positions will produce slightly differing spectra but the inner central region will be bright and thus will dominate.

data are compiled from multiple observing programs (see §2.1) and they consist of both spectral mapping and staring observations, with differing exposure times. As an example, in Fig. 2 we project the SH and LH apertures onto a galaxy in our sample (NGC 0278), showing the two differing nod positions.

Many of the objects in our sample do not have dedicated off-source observations. However, as we only require emission-line flux measurements no background subtraction was necessary for the observations (see §7.2.5.2 of the *Spitzer*-IRS Observers Manual).⁴ Furthermore, the targets are bright compared to the background and therefore any background corrections would be small.

For the reduction of the IRS-staring data, Basic Calibrated Data (BCD) images were co-added and mean averaged at each nod position. Few of the observations were pre-processed with the same *Spitzer* pipeline version. Therefore, to ensure consistency, we extracted the spectra of each galaxy using a custom pipeline based on the *Spitzer* data reduction packages IRSCLEAN (to apply individual custom bad-pixel masks for each of the BCDs) and SPICE (to extract full slit spectra using the latest flux calibration files: version 17.2). For further information on the high-resolution *Spitzer*-IRS pre-processing pipeline, see Chapter 7 of the *Spitzer* Observers Manual.

⁴ The *Spitzer*-IRS Observers Manual is available at <http://ssc.spitzer.caltech.edu/irs/dh/>

Table 3. Mid-IR Spectral Emission Lines (10^{-14} erg s $^{-1}$ cm $^{-2}$)

Common Name	EW PAH λ 11.3 μ m (μ m)	[NeII] λ 12.81 μ m 21.6 eV	[NeV] λ 14.32 μ m 97.1 eV	[NeIII] λ 15.56 μ m 41.0 eV	[NeV] λ 24.32 μ m 97.1 eV	[OIV] λ 25.89 μ m 54.9 eV	[FeII] λ 25.99 μ m 7.9 eV	[SIII] λ 33.48 μ m 23.3 eV	[SiII] λ 34.82 μ m 8.2 eV	Mid-IR AGN?
(1)	(2)	(3)	(4)	(5)	(6)	(7)	(8)	(9)	(10)	(11)
ESO 121-G006	0.816	16.48 \pm 0.50	0.65 \pm 0.08	3.24 \pm 0.24	< 0.59	4.57 \pm 0.40	3.03 \pm 0.26	28.59 \pm 2.80	45.88 \pm 1.87	Y
ESO 209-G009	1.127	9.81 \pm 0.59	< 0.26	1.43 \pm 0.20	< 0.12	< 0.29	< 0.99	22.86 \pm 2.53	31.56 \pm 1.70	-
ESO 265-G007	19.155	2.62 \pm 0.32	< 0.41	1.13 \pm 0.23	< 1.18	< 1.04	1.59 \pm 0.17	8.47 \pm 0.92	11.83 \pm 1.08	-
IC 2056	1.072	12.77 \pm 0.26	< 0.16	2.15 \pm 0.15	< 0.10	0.75 \pm 0.16	2.95 \pm 0.21	42.00 \pm 6.98	52.60 \pm 2.00	-
IC 342	0.498	669.38 \pm 5.01	< 0.64	39.21 \pm 0.73	< 13.71	< 6.83	60.45 \pm 4.95	652.93 \pm 18.77	953.15 \pm 13.71	-
IIZW40	0.015	6.04 \pm 1.12	< 0.28	117.34 \pm 2.34	< 1.14	8.49 \pm 2.28	1.92 \pm 0.49	86.92 \pm 2.02	36.05 \pm 1.41	-
M 82	0.843	506.22 \pm 45.04	< 0.89	80.98 \pm 1.99	< 14.65	45.67 \pm 6.61	137.77 \pm 0.66	1812.90 \pm 36.79	2166.00 \pm 25.52	-
NGC 0253	0.295	3099.10 \pm 126.60	< 5.13	207.89 \pm 9.05	< 113.68	< 83.66	245.20 \pm 0.93	1463.40 \pm 69.65	2411.80 \pm 64.02	-
NGC 0278	0.851	17.84 \pm 0.37	< 0.07	2.95 \pm 0.16	< 0.59	< 0.62	3.82 \pm 0.64	49.55 \pm 3.37	86.82 \pm 1.07	-
NGC 0613	0.501	130.73 \pm 1.55	0.67 \pm 0.11	15.96 \pm 0.50	3.18 \pm 0.56	9.09 \pm 1.53	12.47 \pm 1.25	84.23 \pm 2.70	162.49 \pm 2.11	Y
NGC 0628	0.175	2.31 \pm 0.36	< 0.15	< 0.08	< 0.46	< 0.13	< 0.11	12.35 \pm 0.94	4.78 \pm 0.40	-
NGC 0660	0.730	379.81 \pm 13.96	3.88 \pm 0.25	37.46 \pm 0.69	< 4.59	28.26 \pm 8.24	22.03 \pm 3.61	250.60 \pm 11.47	435.29 \pm 4.03	Y
NGC 0891	0.364	8.57 \pm 0.78	< 0.04	0.84 \pm 0.07	< 0.62	< 1.03	< 0.84	10.74 \pm 2.02	28.11 \pm 0.92	-
NGC 1055	0.747	26.42 \pm 0.79	< 0.19	2.58 \pm 0.20	< 0.58	1.22 \pm 0.26	3.32 \pm 0.47	28.26 \pm 2.46	71.16 \pm 0.98	-
NGC 1068	0.008	538.34 \pm 37.3	898.04 \pm 42.25	1432.20 \pm 76.87	815.96 \pm 58.78	2066.90 \pm 154.88	169.76 \pm 41.70	378.51 \pm 34.07	616.32 \pm 21.94	Y
NGC 1448	0.378	8.17 \pm 0.72	3.68 \pm 0.29	5.02 \pm 0.12	3.60 \pm 0.62	16.02 \pm 0.49	1.60 \pm 0.26	23.76 \pm 5.08	22.55 \pm 1.13	Y
NGC 1559	0.652	14.88 \pm 0.24	< 0.44	2.34 \pm 0.18	< 0.36	< 0.69	2.91 \pm 0.21	23.25 \pm 4.32	26.00 \pm 0.88	-
NGC 1569	0.089	19.06 \pm 1.28	< 0.38	188.15 \pm 2.69	< 1.37	29.32 \pm 0.16	6.43 \pm 0.27	188.06 \pm 4.38	111.08 \pm 2.59	-
NGC 1792	0.492	23.32 \pm 0.32	0.41 \pm 0.13	2.10 \pm 0.17	< 0.25	0.96 \pm 0.06	3.38 \pm 0.38	31.01 \pm 0.93	57.43 \pm 0.72	Y
NGC 1808	0.682	177.36 \pm 16.36	< 0.91	17.26 \pm 0.68	< 8.38	< 9.54	16.62 \pm 2.78	205.83 \pm 20.27	354.26 \pm 15.15	-
NGC 2681	0.883	6.88 \pm 0.28	< 0.15	3.43 \pm 0.21	< 0.36	2.17 \pm 0.70	1.56 \pm 0.43	< 4.01	7.77 \pm 0.66	-
NGC 2903	0.699	181.62 \pm 13.59	< 0.82	13.52 \pm 0.18	< 0.94	< 1.70	13.38 \pm 2.73	124.25 \pm 1.85	298.89 \pm 2.03	-
NGC 3059	0.882	26.79 \pm 0.93	< 0.18	3.13 \pm 0.25	< 0.69	< 1.48	4.07 \pm 0.64	40.41 \pm 5.92	59.18 \pm 0.82	-
NGC 3175	0.752	34.08 \pm 0.46	< 0.35	2.46 \pm 0.22	< 0.86	1.15 \pm 0.07	3.91 \pm 1.54	71.51 \pm 2.47	92.40 \pm 1.28	-
NGC 3184	0.324	5.70 \pm 0.15	< 0.10	0.67 \pm 0.08	< 0.20	0.50 \pm 0.09	< 0.27	4.31 \pm 0.35	5.05 \pm 0.52	-
NGC 3198	0.423	4.75 \pm 0.11	< 0.03	0.30 \pm 0.08	< 0.16	0.45 \pm 0.10	< 0.31	3.39 \pm 0.45	4.34 \pm 0.59	-
NGC 3351	0.263	18.87 \pm 1.09	< 0.13	1.71 \pm 0.08	< 0.14	4.71 \pm 3.19	2.91 \pm 0.32	38.47 \pm 1.41	70.25 \pm 1.19	-
NGC 3368	0.488	4.29 \pm 0.29	< 0.29	2.85 \pm 0.25	< 0.74	0.99 \pm 0.29	2.58 \pm 0.12	< 5.88	13.22 \pm 2.53	-
NGC 3511	0.647	6.37 \pm 0.18	< 0.34	1.39 \pm 0.11	< 0.64	< 1.11	< 1.25	20.19 \pm 3.06	31.35 \pm 0.79	-
NGC 3521	0.172	3.02 \pm 0.22	< 0.11	1.77 \pm 0.17	< 0.31	1.53 \pm 0.11	< 0.82	7.14 \pm 1.08	21.79 \pm 1.11	-
NGC 3556	0.771	26.43 \pm 1.79	< 0.26	3.44 \pm 0.11	< 0.32	< 0.69	2.79 \pm 0.18	100.28 \pm 1.09	95.50 \pm 1.14	-
NGC 3621	0.555	3.69 \pm 0.16	0.29 \pm 0.00	1.51 \pm 0.16	0.53 \pm 0.05	2.86 \pm 0.39	0.86 \pm 0.73	12.27 \pm 0.62	17.66 \pm 1.08	Y
NGC 3627	0.579	8.14 \pm 0.29	0.30 \pm 0.08	2.79 \pm 0.15	0.47 \pm 0.04	1.99 \pm 0.53	1.30 \pm 0.28	5.78 \pm 0.96	16.84 \pm 1.90	Y
NGC 3628	0.798	155.28 \pm 8.38	0.95 \pm 0.06	10.38 \pm 0.19	< 2.39	5.35 \pm 2.89	12.12 \pm 0.27	155.61 \pm 6.44	264.07 \pm 2.31	Y
NGC 3675	0.588	8.07 \pm 0.13	< 0.23	2.21 \pm 0.20	< 0.48	< 0.58	< 1.39	12.65 \pm 3.29	25.12 \pm 0.89	-
NGC 3726	1.408	5.47 \pm 0.13	< 0.41	0.43 \pm 0.06	< 0.52	< 0.44	< 0.45	12.60 \pm 0.11	11.82 \pm 0.27	-
NGC 3938	0.314	1.43 \pm 0.14	< 0.09	0.31 \pm 0.09	< 0.14	< 0.29	< 0.17	3.20 \pm 0.29	9.84 \pm 2.57	-
NGC 3949	0.528	5.82 \pm 0.29	< 0.11	1.11 \pm 0.15	< 0.11	1.48 \pm 0.67	1.15 \pm 0.03	17.12 \pm 1.28	29.25 \pm 0.89	-
NGC 4013	0.639	13.12 \pm 0.26	< 0.09	2.77 \pm 0.24	< 0.89	< 1.01	< 2.44	13.49 \pm 2.33	34.23 \pm 0.90	-
NGC 4051	0.085	16.78 \pm 0.48	11.26 \pm 0.43	16.02 \pm 0.47	11.82 \pm 1.20	36.42 \pm 2.41	< 1.93	13.74 \pm 1.17	17.17 \pm 1.73	Y

Table 3 – continued

Common Name	EW PAH $\lambda 11.3 \mu\text{m}$ (μm)	[NeII] $\lambda 12.81 \mu\text{m}$ 21.6 eV	[NeV] $\lambda 14.32 \mu\text{m}$ 97.1 eV	[NeIII] $\lambda 15.56 \mu\text{m}$ 41.0 eV	[NeV] $\lambda 24.32 \mu\text{m}$ 97.1 eV	[OIV] $\lambda 25.89 \mu\text{m}$ 54.9 eV	[FeII] $\lambda 25.99 \mu\text{m}$ 7.9 eV	[SIII] $\lambda 33.48 \mu\text{m}$ 23.3 eV	[SiII] $\lambda 34.82 \mu\text{m}$ 8.2 eV	Mid-IR AGN?
(1)	(2)	(3)	(4)	(5)	(6)	(7)	(8)	(9)	(10)	(11)
NGC 4085	1.159	23.03 ± 0.31	< 0.15	2.92 ± 0.21	< 0.92	< 0.44	1.91 ± 0.43	36.63 ± 2.09	53.22 ± 1.66	-
NGC 4088	0.575	43.67 ± 1.61	< 0.19	2.54 ± 0.13	< 0.47	< 0.53	1.69 ± 0.31	36.31 ± 0.80	61.27 ± 0.59	-
NGC 4157	0.832	11.63 ± 0.18	< 0.07	1.44 ± 0.12	< 0.70	1.10 ± 0.32	2.51 ± 0.75	29.70 ± 3.13	54.72 ± 2.79	-
NGC 4490	0.396	3.55 ± 0.45	< 0.10	3.50 ± 0.12	< 0.10	1.08 ± 0.17	1.75 ± 0.35	16.87 ± 2.97	22.26 ± 0.87	-
NGC 4536	0.434	35.46 ± 0.39	< 0.06	6.11 ± 0.06	< 0.13	1.72 ± 0.25	9.74 ± 1.50	100.48 ± 4.53	114.02 ± 1.53	-
NGC 4559	0.214	1.89 ± 0.13	< 0.05	0.53 ± 0.08	< 0.07	< 1.62	0.54 ± 0.15	10.61 ± 0.93	10.03 ± 0.44	-
NGC 4631	0.647	45.92 ± 0.71	< 0.07	10.15 ± 0.13	< 0.27	< 1.47	< 3.67	85.16 ± 0.76	114.74 ± 1.89	-
NGC 4666	0.517	35.65 ± 2.01	< 0.57	8.32 ± 0.15	< 0.89	6.77 ± 1.94	5.14 ± 0.32	68.92 ± 1.84	124.15 ± 2.25	-
NGC 4736	0.734	3.74 ± 0.34	< 0.12	4.25 ± 0.07	< 0.76	2.01 ± 0.36	3.22 ± 0.44	6.38 ± 1.50	20.28 ± 1.13	-
NGC 4818	0.314	195.95 ± 14.93	< 0.38	13.37 ± 0.73	< 1.62	< 4.39	8.86 ± 0.50	86.31 ± 3.67	125.45 ± 3.74	-
NGC 4945	0.712	698.41 ± 60.43	7.06 ± 0.31	68.07 ± 2.27	< 2.12	28.35 ± 1.39	49.26 ± 13.00	359.62 ± 20.42	732.76 ± 7.84	Y
NGC 5033	0.644	13.26 ± 0.18	0.42 ± 0.05	5.08 ± 0.15	0.48 ± 0.08	5.08 ± 0.51	2.02 ± 0.47	17.38 ± 0.85	45.35 ± 1.52	Y
NGC 5055	0.606	6.04 ± 0.22	< 0.11	3.08 ± 0.10	< 0.89	1.75 ± 0.16	2.19 ± 0.47	11.90 ± 0.65	34.10 ± 1.84	-
NGC 5128	0.165	202.71 ± 3.97	21.96 ± 0.88	149.98 ± 5.04	27.88 ± 0.71	123.63 ± 2.72	24.99 ± 5.72	140.69 ± 6.05	297.43 ± 1.52	Y
NGC 5194	0.591	17.03 ± 0.26	0.74 ± 0.10	10.91 ± 0.24	1.61 ± 0.11	7.93 ± 0.25	4.33 ± 0.87	18.39 ± 0.81	60.42 ± 2.08	Y
NGC 5195	0.842	5.54 ± 0.72	0.20 ± 0.06	2.17 ± 0.11	< 0.39	0.94 ± 0.23	< 0.96	3.22 ± 0.39	12.21 ± 1.26	Y
NGC 5236	0.602	503.33 ± 19.88	< 0.61	29.30 ± 0.77	< 1.19	5.75 ± 1.08	18.57 ± 3.42	263.50 ± 9.21	391.40 ± 8.55	-
NGC 5643	0.227	46.41 ± 3.56	24.63 ± 1.03	56.47 ± 1.16	31.33 ± 1.77	118.28 ± 4.74	< 4.00	33.26 ± 3.05	42.67 ± 2.84	Y
NGC 5907	0.791	6.07 ± 0.22	< 0.01	1.28 ± 0.16	< 0.07	1.57 ± 0.51	0.94 ± 0.20	14.21 ± 1.41	23.94 ± 0.60	-
NGC 6300	0.125	11.52 ± 0.63	12.54 ± 0.66	15.28 ± 0.57	8.33 ± 1.29	29.45 ± 2.26	< 3.49	< 7.63	11.31 ± 0.82	Y
NGC 6744	0.245	1.06 ± 0.26	< 0.03	1.53 ± 0.17	< 0.13	< 0.73	0.84 ± 0.25	3.57 ± 0.98	3.24 ± 0.41	-
NGC 6946	0.768	38.45 ± 0.66	< 0.17	3.77 ± 0.10	< 0.59	4.00 ± 0.68	8.42 ± 0.60	61.00 ± 3.70	112.25 ± 1.57	-
NGC 7331	0.337	4.47 ± 0.15	< 0.16	3.08 ± 0.10	< 0.39	1.88 ± 0.14	1.61 ± 0.28	13.81 ± 0.41	30.58 ± 0.93	-
UGCA 127	0.982	9.34 ± 0.38	< 0.15	1.53 ± 0.24	< 0.97	3.37 ± 0.16	3.43 ± 0.12	29.37 ± 2.41	44.08 ± 1.68	-

NOTES: (1) Common galaxy name. (2) Equivalent width of the 11.3 μm PAH feature in units of μm . (3–10) Fluxes and their statistical uncertainties for the measured mid-IR narrow emission lines in units $10^{-14} \text{ erg cm}^{-2} \text{ s}^{-1}$. The mean uncertainty of the fluxes is approximately 10 percent. 3σ upper limits are quoted for non-detections. (11) Mid-IR AGN on the basis of [NeV] $\lambda 14.32 \mu\text{m}$ emission.

For the reduction of the IRS-spectral mapping data, custom bad-pixel masks were again applied to the BCD images. CUBISM (Smith et al. 2007) was then used in conjunction with the latest flux calibration files to construct final data cubes and extract spectra of the central regions matched to the sizes of projected SH and LH apertures.

After extraction of the raw spectra, the ends of each echelle order were trimmed to remove the additional spectral noise caused by the poor response of the grating.⁵ Using the redshifts given in the RBGS, each extracted spectrum was shifted to rest-wavelength for further spectral analysis.

Solely for presentation purposes, single continuous spectra of each slit were produced. Echelle orders were matched by fitting each spectral continuum from a given order with either a first or second order polynomial. Each echelle order continuum was then combined by matching and calibrating to the 1st echelle order of the relevant slit to construct the final SH and LH continua. Due to the different aperture sizes (and hence continuum fluxes), we have not attempted to match the SH and LH spectra. Fig. 11 shows the reduced spectra for each of the sources using the SH and LH slits (left and right panels respectively).

2.3 Measuring Emission-line Properties

Second-order polynomials were used to model the continuum and gaussian profiles were simultaneously fit to spectral features to determine emission-line fluxes. These were calculated using the IDL-based spectral analysis tool SMART (Higdon et al. 2004).⁶ Fluxes or 3σ upper-limits are given in Table 3 for the following emission lines: [NeII] $\lambda 12.81 \mu\text{m}$, [NeV] $\lambda 14.32 \mu\text{m}$, [NeIII] $\lambda 15.56 \mu\text{m}$, [NeV] $\lambda 24.32 \mu\text{m}$, [OIV] $\lambda 25.89 \mu\text{m}$, [FeII] $\lambda 25.99 \mu\text{m}$, [SIII] $\lambda 33.48 \mu\text{m}$ and [SiII] $\lambda 34.82 \mu\text{m}$. Polycyclic Aromatic Hydrocarbon (PAH; e.g., Draine 2003) features are detected in many of the galaxies; we use the $11.3 \mu\text{m}$ PAH equivalent width in our analyses and report these values in Table 3. Due to their broad profiles, the strength of the PAH features are measured using multiple gaussians. The results obtained from our continuum and emission-line fitting procedure are shown in Fig. 3 for all [NeV] $\lambda 14.32 \mu\text{m}$ detected galaxies.

Of the 64 galaxies in the $D < 15$ Mpc sample, 16 have published *Spitzer*-IRS data in S08 and 18 have published *Spitzer*-IRS data in Dale et al. (2009; hereafter D09). However, due to differing data-reduction routines and approaches in the detection of emission lines (e.g., we measured emission-line properties in apertures centred on the near-IR nucleus, S08 searched for emission lines in small apertures across the circumnuclear region of each galaxy, and D09 constrained emission-line properties in large apertures across the extent of each galaxy), we have re-analysed all of the galaxies to provide self-consistent results. However, despite these differing approaches, we find average emission-line flux variances of only ≈ 10 –30% between our study and that of S08 and D09 for those galaxies with with detected [NeII] $\lambda 12.81 \mu\text{m}$, [NeIII] $\lambda 15.56 \mu\text{m}$, and [OIV] $\lambda 25.89 \mu\text{m}$

emission; when comparing to D09 we scaled our emission-line fluxes by the difference in aperture size between D09 and our study.

3 RESULTS

3.1 The Discovery of a Significant Population of Optically Unidentified AGNs

Of the 64 objects in our $D < 15$ Mpc sample (presented in Tables 1 and 3), 17 have 3σ detections of the [NeV] $\lambda 14.32 \mu\text{m}$ emission line, and therefore have unambiguous evidence for AGN activity.⁷ We therefore find an overall AGN fraction of $\approx 27_{-6}^{+8}$ percent in the most bolometrically luminous galaxies to $D < 15$ Mpc ($L_{\text{IR}} \approx (0.3 - 20) \times 10^{10} L_{\odot}$).⁸

Of the 16 galaxies in common between S08 and our sample, S08 identified [NeV] (14.32 or $24.32 \mu\text{m}$) in four systems (NGC 3556; NGC 3938; NGC 4536; NGC 5055). We do not detect significant [NeV] in any of these four galaxies, which may be due to differences in the positions and sizes of the apertures used to extract the spectra within CUBISM. Of the 18 galaxies in common between D09 and our sample, D09 identified [NeV] $\lambda 14.32 \mu\text{m}$ in three systems (NGC 3621; NGC 5033; NGC 5194), all of which we also identify here; however, we also identified [NeV] emission in two systems where D09 quote [NeV] upper limits (NGC 3627; NGC 5195), which could be due to dilution of the [NeV] emission by the host galaxy in the large apertures used by D09. We note that differences in the identification of weak [NeV] emission can also be due to the adopted emission-line detection procedure and signal-to-noise ratio threshold.

Seven ($\approx 11_{-4}^{+6}$ percent) of the 64 galaxies in our sample are unambiguously identified as AGNs using classical optical emission-line diagnostics (i.e., optically classified as Seyfert galaxies; e.g., Baldwin et al. 1981; Veilleux & Osterbrock 1987; Kauffmann et al. 2003); see Table 1. All of these optically identified AGNs are classified as AGNs at mid-IR wavelengths in our analysis. In Fig. 4, we plot the optical emission-line ratios of the 53 galaxies with good-quality optical spectra; of the other 11 galaxies in the sample, three do not have a sufficient number of detected emission lines to classify at optical wavelengths using emission-line diagnostics, and eight do not have published optical spectroscopy. Ten of our mid-IR classified AGNs are not unambiguously identified as AGNs at optical wavelengths: five are classified as HII galaxies (NGC 0613, NGC 1448, NGC 1792, NGC 4945, and NGC 5128), four are classified as LINERS (NGC 0660, NGC 3627, NGC 3628, and NGC 5195), and one does not have good-quality optical spectroscopic data

⁷ Theoretical modeling has shown that [NeV] can also be produced in galaxies containing a large population of Wolf-Rayet (WR) stars (Schaerer & Stasińska 1999). Two WR galaxies are present in our volume-limited sample (IIZw40 and NGC 1569). However, [NeV] emission is not detected in either source, and their mid-IR continuum and spectral features are clearly distinct from those of AGNs.

⁸ Small-number Poisson statistical errors are calculated for upper and lower limits based on the 1σ confidence levels given in Gehrels (1986).

⁵ Wavelength trim ranges are given in Table 5.1 of the *Spitzer*-IRS Observers Manual.

⁶ SMART was developed by the IRS Team at Cornell University and is available through the *Spitzer* Science Center at Caltech.

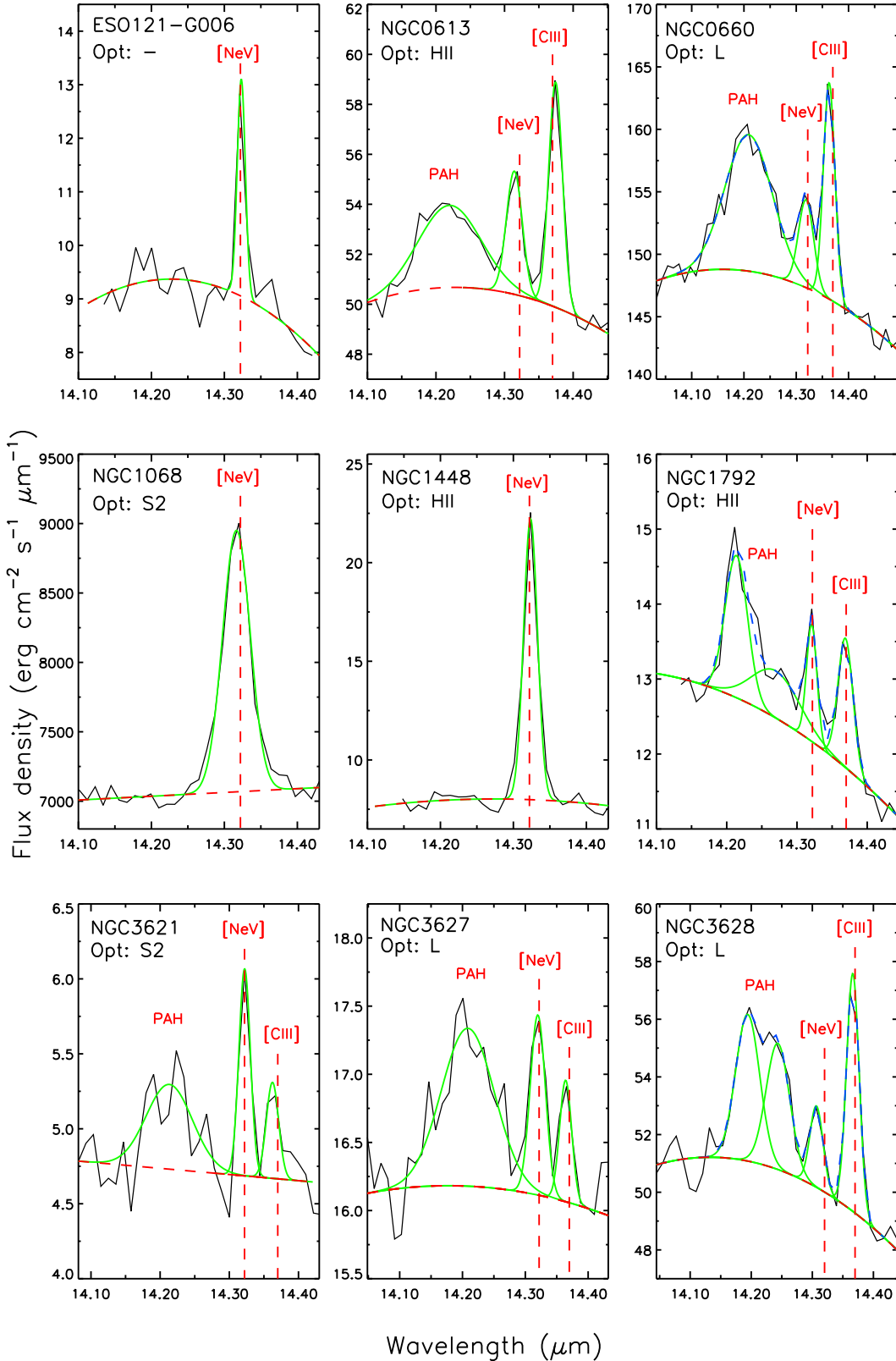


Figure 3. Mid-IR spectra expanded around the [NeV] $\lambda 14.32 \mu\text{m}$ emission-line region for all [NeV] detected galaxies covering a broad range of optical and mid-IR spectral properties. The dotted line indicates the second-order polynomial fit to the continuum and the solid lines indicate the gaussian fit to the emission-line features; the [NeV] $\lambda 14.32 \mu\text{m}$, $\lambda 14.2 \mu\text{m}$ PAH, and [CIII] $\lambda 14.37 \mu\text{m}$ emission features are labeled when detected. The identification of AGN activity from the [NeV] $\lambda 14.32 \mu\text{m}$ emission-line in ten objects is complicated by the PAH and [CIII] star-forming signatures and thus high signal-to-noise data is required.

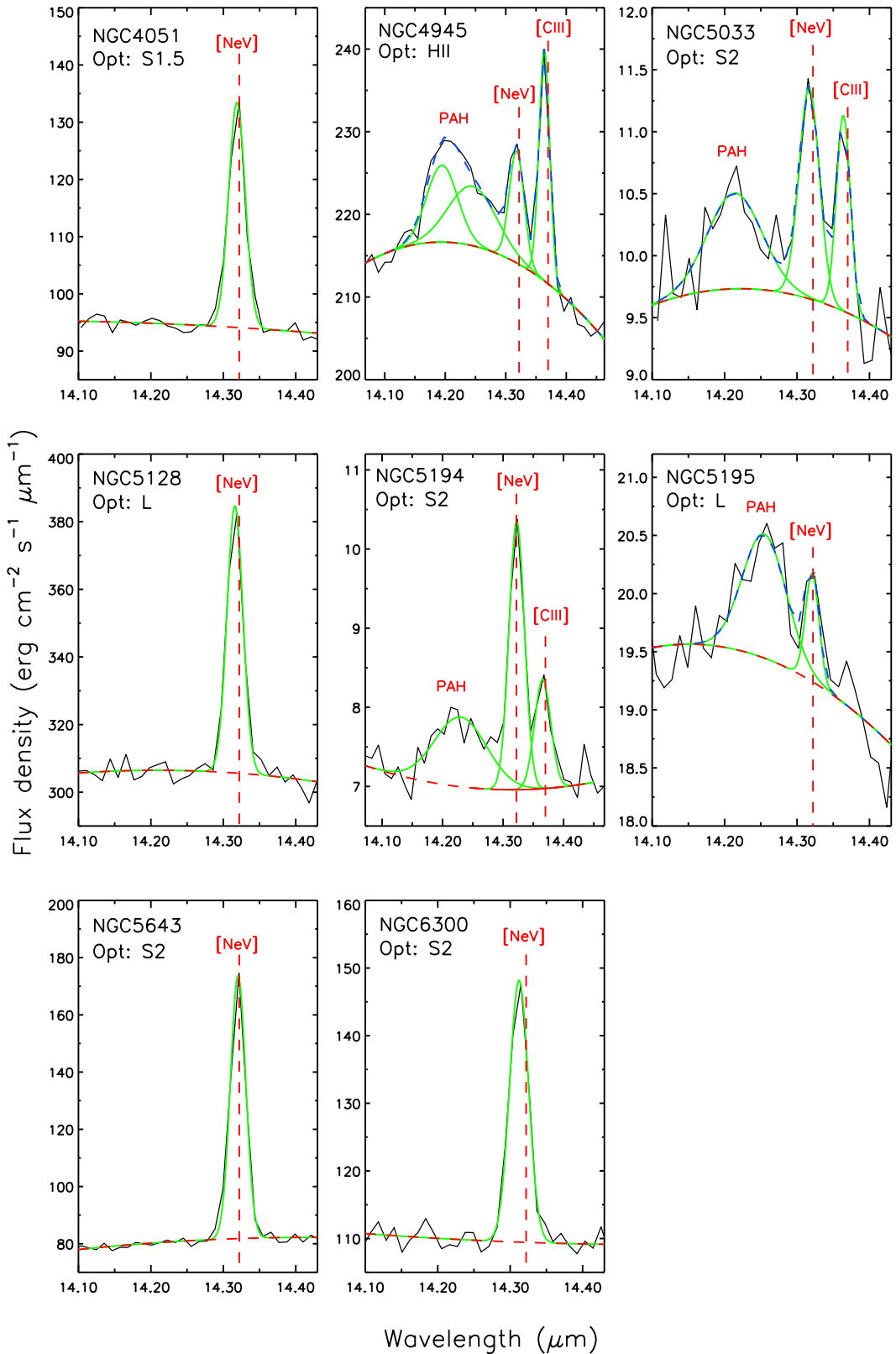


Figure 3 – continued

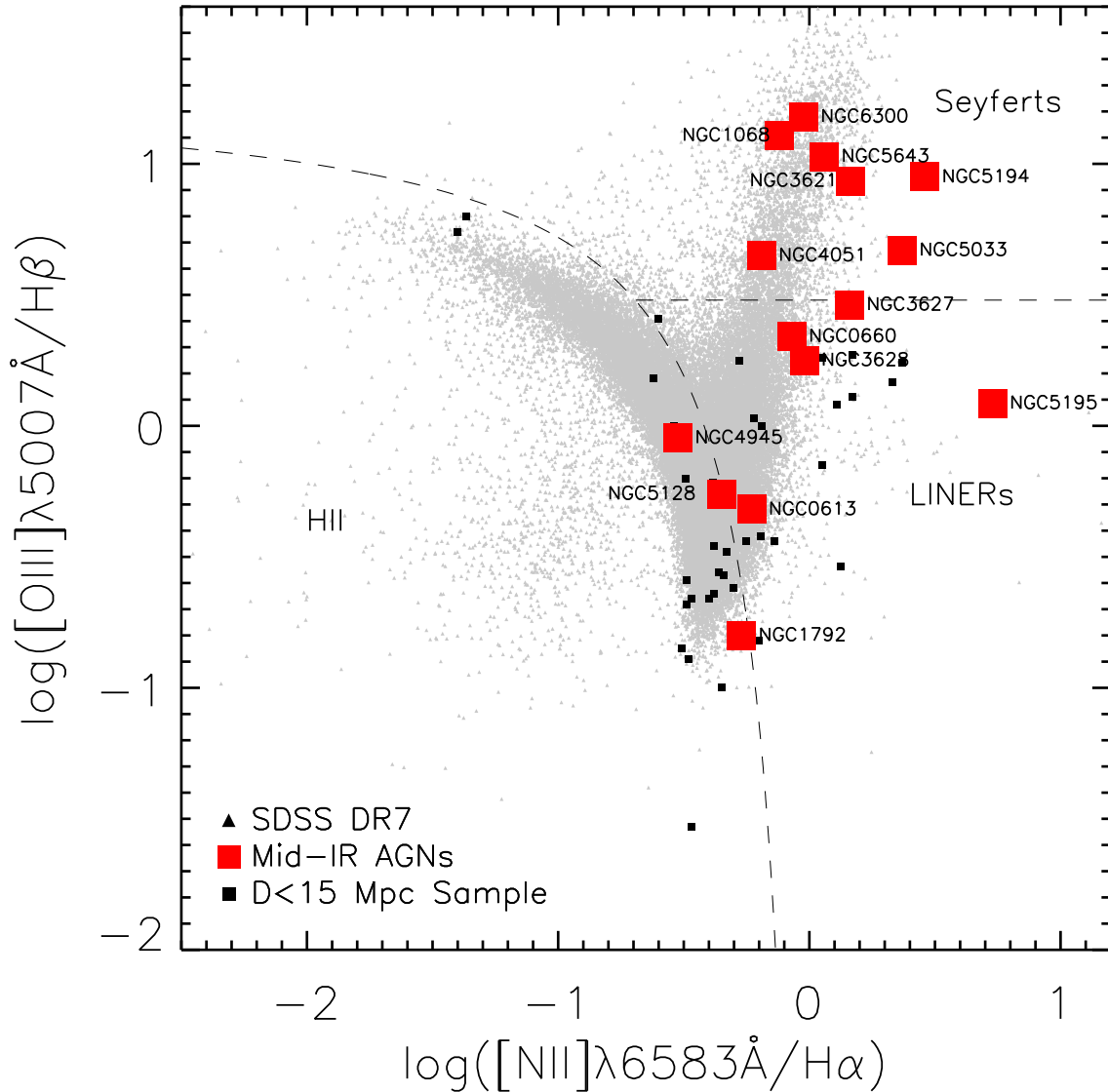


Figure 4. Emission-line diagnostic diagram showing $[OIII]\lambda 5007\text{\AA}/H\beta$ versus $[NII]\lambda 6583\text{\AA}/H\alpha$ for our $D < 15$ Mpc galaxy sample (squares) and the Seventh Data Release of SDSS (dots). Kauffmann et al. (2003) demarcation lines are shown to isolate the Seyfert, LINER and star-forming HII regions (dashed lines). Those galaxies with 3σ [NeV] $\lambda 14.32\ \mu\text{m}$ detections (i.e., mid-IR identified AGNs) are labeled and highlighted with large squares. Seven of the $D < 15$ Mpc galaxies are optically classified as Seyferts, all of which are identified as mid-IR AGNs, while the other objects are optically classified either as HII galaxies or LINERS. Two additional mid-IR AGNs (NGC 1448; ESO121-G006) are not shown in the figure. NGC 1448 is classified as an HII galaxy (Veron-Cetty et al. 1986) but cannot be plotted on this figure since both $[OIII]\lambda 5007$ and $H\beta$ are undetected. ESO121-G006 lacks good-quality optical spectroscopy but since it is hosted in a highly inclined galaxy, it is likely to be an optically unidentified AGN; see §3.3 and Fig. 8.

(ESO121-G006). Although ESO121-G006 does not have a good-quality optical spectrum, since it is hosted in a highly inclined galaxy we would expect it to be an optically unidentified AGN; see §3.3 and Fig. 8. Large optical spectroscopic studies (e.g., Veilleux et al. 1995; Ho97) have speculated that the central regions of many LINERS are likely to be powered by AGN activity. Indeed, using *Chandra* X-ray observations, Ho et al. (2001) suggest ≈ 60 percent of all LINERS host AGNs. By contrast, using our mid-IR diagnostics, we find only ≈ 25 percent of IR-bright LINERS appear to be AGNs,

which could be due to a number of factors (e.g., different sample selection and ambiguous evidence for AGN activity at X-ray energies; i.e., X-ray binaries).

The optical spectroscopy for the galaxies in our sample comes from a variety of different studies with a range in emission-line sensitivities. However, the majority of the galaxies are in Ho97, which arguably comprises the most sensitive optical spectroscopy of a large number of nearby galaxies. Of the 38 galaxies present in both our sample and Ho97, we find that eight are mid-IR identified AGNs (NGC 0660,

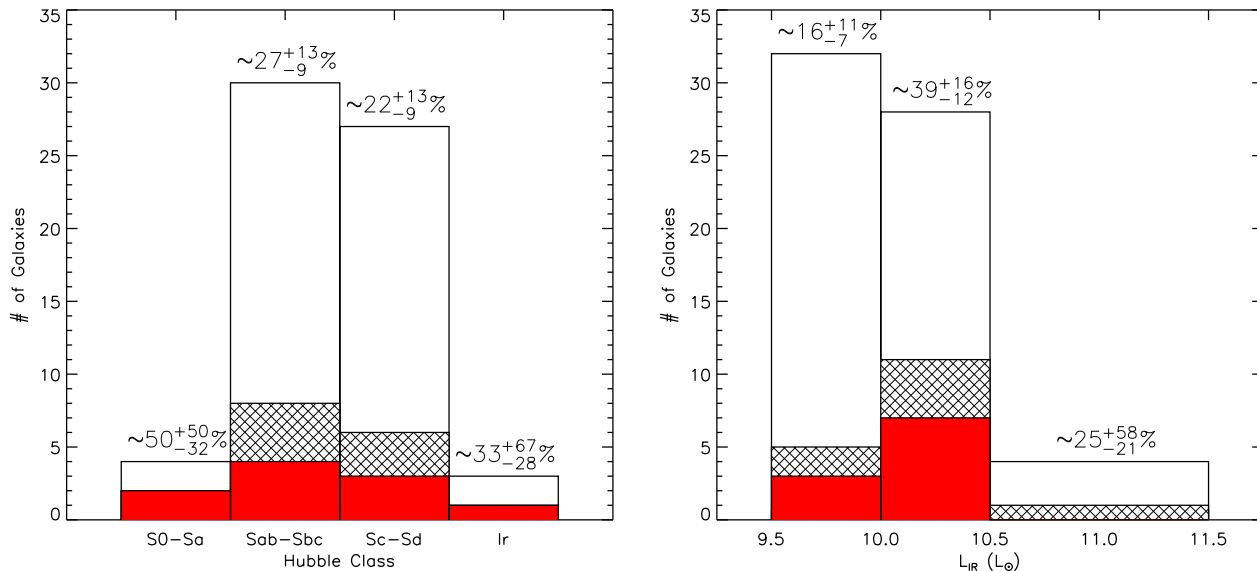


Figure 5. Fraction of AGNs identified in the $D < 15$ Mpc sample shown as a function of host-galaxy morphological classification and IR luminosity; the AGN fraction and associated 1σ errors are given for each sample bin. We further sub-divide the AGNs into [NeV] $\lambda 14.32$ μm detected sources which are also optically observed to have AGN signatures (cross hatching), [NeV] $\lambda 14.32$ μm detected sources which lack optical AGN signatures (solid colour), and combining these to give all galaxies with detected [NeV] $\lambda 14.32$ μm emission, i.e. total number of AGN (cross-hatch+solid colour).

NGC 1068, NGC 3627, NGC 3628, NGC 4051, NGC 5033, NGC 5194 and NGC 5195), only four of which are unambiguously identified as AGN at optical wavelengths. One of the optically unidentified AGNs is NGC 5195, which may be a binary AGN system with NGC 5194 in the Whirlpool galaxy. Potential AGN activity has also been found in NGC 5195 using *Chandra* observations (Terashima & Wilson 2004).

Optical spectroscopic surveys have found that AGNs typically reside in moderately massive bulge-dominated galaxies (Hubble-type: E-Sbc; $M_* \approx (0.1-3) \times 10^{11} M_{\odot}$; e.g., Ho97; Heckman et al. 2004). In Fig. 5 we show the histogram of galaxy morphology for our $D < 15$ Mpc sample. We find that the host galaxies of our mid-IR identified AGNs cover a wide range of galaxy type (S0-Ir). However, in contrast to Ho97 and Heckman et al. (2004), we find that a large fraction of Sc-Sd-type galaxies host AGN activity at mid-IR wavelengths ($\approx 22^{+13}_{-9}$ percent; i.e., a comparable AGN fraction to that found in Sab-Sbc galaxies). This shows that late-type galaxies typically assumed to host pseudo bulges (Sc-Sd) can harbour AGN activity, and therefore must host a SMBH. As found in previous studies, this indicates that galaxies without classical bulges can host SMBHs (e.g., Greene et al. 2008; Barth et al. 2009).

In Fig. 5 we also show the incidence of AGN activity as a function of IR luminosity. In the moderate-luminosity IR bin ($L_{\text{IR}} \approx (1-3) \times 10^{10} L_{\odot}$), we find a large AGN fraction of $\approx 39^{+16}_{-12}$ percent, suggesting that the overall AGN fraction for our sample may be a lower limit. The smaller AGN fractions found in the lower ($L_{\text{IR}} < 10^{10} L_{\odot}$; $\approx 16^{+11}_{-7}$ percent) and higher ($L_{\text{IR}} > 3 \times 10^{10} L_{\odot}$; $\approx 25^{+58}_{-21}$ percent) IR luminosity bins could be due to relatively weaker AGN sensitivity limits (i.e., a higher $L_{[\text{NeV}]} / L_{\text{IR}}$ emission-line ratio) and large uncertainties due to small-number statistics,

respectively. Indeed, we find similar AGN fractions (of order ≈ 10 percent) in both the lower IR luminosity and moderate IR luminosity bins if we only consider AGNs identified with $L_{[\text{NeV}]} / L_{\text{IR}} < 10^{-5}$, suggesting that further AGNs remain to be detected in the lower IR luminosity; see Fig. 6a. This may indicate that the overall AGN fraction in our IR-bright sample may be closer to ≈ 40 percent.

The large AGN fraction found in our study indicates a tighter connection between AGN activity and IR luminosity for galaxies in the local Universe than previously found, exceeding the AGN fraction obtained with optical spectroscopy by up-to an order of magnitude (e.g., compared to the results for $L_{\text{IR}} < 10^{11} L_{\odot}$ galaxies in Veilleux et al. 1999). This may indicate a close association between AGN activity and star formation, as is typically expected given the tight relationship between SMBH and spheroid mass in the local Universe (e.g., Magorrian et al. 1998; Gebhardt et al. 2000). There are probably two reasons why we identify a significantly larger AGN fraction than previously found: (1) mid-IR spectroscopy provides a more sensitive probe of AGN activity than optical spectroscopy, and (2) our galaxies are very nearby, allowing us to identify faint AGN signatures.

3.2 Why are AGN signatures often absent at optical wavelengths?

Of the seventeen galaxies in our $D < 15$ Mpc sample that unambiguously host AGN activity, ten ($\approx 60^{+25}_{-18}$ percent) lack AGN signatures at optical wavelengths. Here we explore the three most likely reasons why the AGN signatures are absent in the optical spectra of these galaxies: (1) the optically unidentified AGNs are intrinsically lower luminosity systems, (2) the optically unidentified AGNs have a larger

fraction of star formation/stellar light that dilutes the optical AGN signatures, or (3) the optically unidentified AGNs are more heavily obscured at optical wavelengths.

3.2.1 Are optically unidentified AGNs intrinsically low luminosity?

The non detection of optical AGN signatures in the optically unidentified AGNs may be due to the AGNs being lower luminosity systems. In Fig. 7a, we show the [NeV] λ 14.32 μ m luminosities of the mid-IR identified AGNs and a sample of well-studied local AGNs from Panessa et al. (2006) as a function of their [OIII] λ 5007 \AA luminosity. We characterise the [NeV]–[OIII] luminosity relationship using a regressional fit.⁹

$$\log[\text{NeV}] = (1.19 \pm 0.12) \log[\text{OIII}] - (8.65 \pm 4.60) \quad (1)$$

The tightness in the [NeV]–[OIII] luminosity relationship indicates that the [NeV] luminosity provides a reliable measurement of the intrinsic luminosity of the AGN; the optically identified AGNs lie on this relationship if we correct the [OIII] luminosity for extinction as measured using the Balmer decrement (see §3.2.3).

The optically identified AGNs in our sample cover a broader range of [NeV] λ 14.32 μ m luminosities than the optically unidentified AGNs ($L_{[\text{NeV}]} \approx 10^{37}$ – 10^{41} erg s^{-1} and $L_{[\text{NeV}]} \approx 10^{37}$ – 10^{39} erg s^{-1} , respectively). However, since there are optically identified AGNs with similar luminosities to the optically unidentified AGNs, this indicates that the dominant reason for the non detection of the optically unidentified AGNs cannot be due to them hosting intrinsically lower-luminosity AGN activity. Fig. 7a also shows that the non identification of optical AGN signatures in the optically unidentified AGNs is not due to low-sensitivity optical spectroscopy since the [OIII]/[NeV] luminosity ratios are lower than that given in Equation 1.

3.2.2 Are optically unidentified AGNs star-formation dominated?

The non-identification of AGNs at optical wavelengths could be due to dilution from star-formation signatures, which we can test with our data. The mid-IR continua of starburst galaxies are typically characterised by strong PAH features at $\lambda \sim 3.3, 6.2, 7.7, 8.6, 11.3, 12.7, 14.2$ and $17.0 \mu\text{m}$ combined with a steep spectral slope at far-IR ($\lambda > 25 \mu\text{m}$) wavelengths (Brandl et al. 2006). By contrast, PAH features tend to be weak or absent in AGN-dominated systems (e.g., NGC 1068; Rigopoulou et al. 2002). It is apparent from the *Spitzer*-IRS spectroscopy presented in Fig. 3 and 11, that most of the optically unidentified AGNs exhibit star-formation signatures at mid-IR wavelengths, indicating that they host joint AGN–starburst activity. However, to test whether the lack of AGN signatures at optical wavelengths is due to dilution from star-formation, we need to compare the relative AGN–star-formation contributions for both the optically identified and unidentified AGNs.

As the sources in the sample are well resolved, we

can use the *Spitzer*-IRS spectra to quantify the relative strengths of the star-formation and AGN activity in the circumnuclear regions of the mid-IR identified AGNs. Previous studies have shown that the equivalent width of the IR-detected PAH features at 6.2 and 7.7 μm are well correlated with the AGN–starburst activity occurring within a galaxy (e.g., Genzel et al. 1998; Laurent et al. 2000; Peeters et al. 2004; Dale et al. 2006). However, given the spectral coverage of the *Spitzer*-IRS spectroscopy for the $D < 15$ Mpc sample ($\lambda \sim 9.9$ – $37.2 \mu\text{m}$), here we calibrate and use the equivalent width of the 11.3 μm PAH feature ($\text{EW}_{11.3,\text{PAH}}$, which is detected in every galaxy) to indicate the relative AGN–star-formation contribution of each galaxy. Martín-Hernández et al. (2006) find that for a starburst-dominated circumnuclear region $\text{EW}_{11.3,\text{PAH}}$ (100 percent SF) $\approx 0.7 \mu\text{m}$. Comparing this to an AGN-dominated system (i.e., NGC 1068) we find $\text{EW}_{11.3,\text{PAH}}$ (100 percent AGN) $\approx 0.008 \mu\text{m}$. The mid-IR emission line ratios can also be used to constrain the relative contributions of AGN and stellar emission (e.g., Dale et al. 2006). Since [NeII] λ 12.82 μm emission is primarily produced by star-formation activity within a galaxy, and [NeV] λ 14.32 μm is solely attributed to AGN activity, the ratio of these emission lines is also a strong tracer of the relative strengths of these two processes (e.g., Sturm et al. 2002).

In Fig. 6b we present the predicted $\text{EW}_{11.3,\text{PAH}}$ and [NeII] λ 12.82 μm – [NeV] λ 14.32 μm flux ratios for different AGN–star-formation contributions; this is similar in principle to Genzel et al. (1998). Both of the AGN–star-formation ratio estimates are in good agreement for the majority of the mid-IR AGNs, with a mean dispersion of ≈ 20 percent. We note that the predicted AGN–star-formation contributions for four (≈ 25 percent) of the galaxies (NGC 1068, NGC 4051, NGC 5128 and NGC 5643) differ by more than a factor of two from the mixing model, whilst the other mid-IR identified AGNs lie within a factor of 40 percent. One of these such outliers is the FR-1 radio galaxy, NGC 5128 ($\text{EW}_{11.3,\text{PAH,model}} > 4 \times \text{EW}_{11.3,\text{PAH,obs}}$), which could be due to dilution of the PAH feature by an underlying synchrotron component (related to the radio emission) that is emitting at mid-IR wavelengths. On the basis of Fig. 6b, the IR emission for five (29^{+20}_{-13} percent) of the mid-IR identified AGNs (NGC 1068, NGC 6300, NGC 4051, NGC 5643 and NGC 1448) has a significant contribution from AGN activity (> 25 percent), only one of which is an optically unidentified AGN (NGC 1448). As may be expected, these five galaxies also host the most luminous AGNs, as shown in Fig. 7a. The IR emission for the other twelve ($\approx 71^{+26}_{-20}$ percent) mid-IR identified AGNs appears to be star-formation dominated (AGN contribution < 25 percent), nine of which are optically unidentified AGNs. These analyses have been performed using the SH module of *Spitzer*-IRS, which traces only the circumnuclear region of these galaxies. However, we get qualitatively similar results if we consider the $L_{[\text{NeV}]} / L_{\text{IR}}$ ratios, which should provide a measure of the contribution of the AGN to the *total* IR luminosity of the galaxy (i.e., as measured by *IRAS*); see Fig. 6a.

On the basis of these analyses we therefore derive qualitatively similar conclusions to those in §3.2.1. Clearly, there is a difference in the distribution of relative AGN–star formation strengths, with the optically unidentified AGNs being typically more star-formation dominated than the opti-

⁹ The fit to the data was obtained using the IDL-based robust bi-sector linefit algorithm ROBUST.LINEFIT.

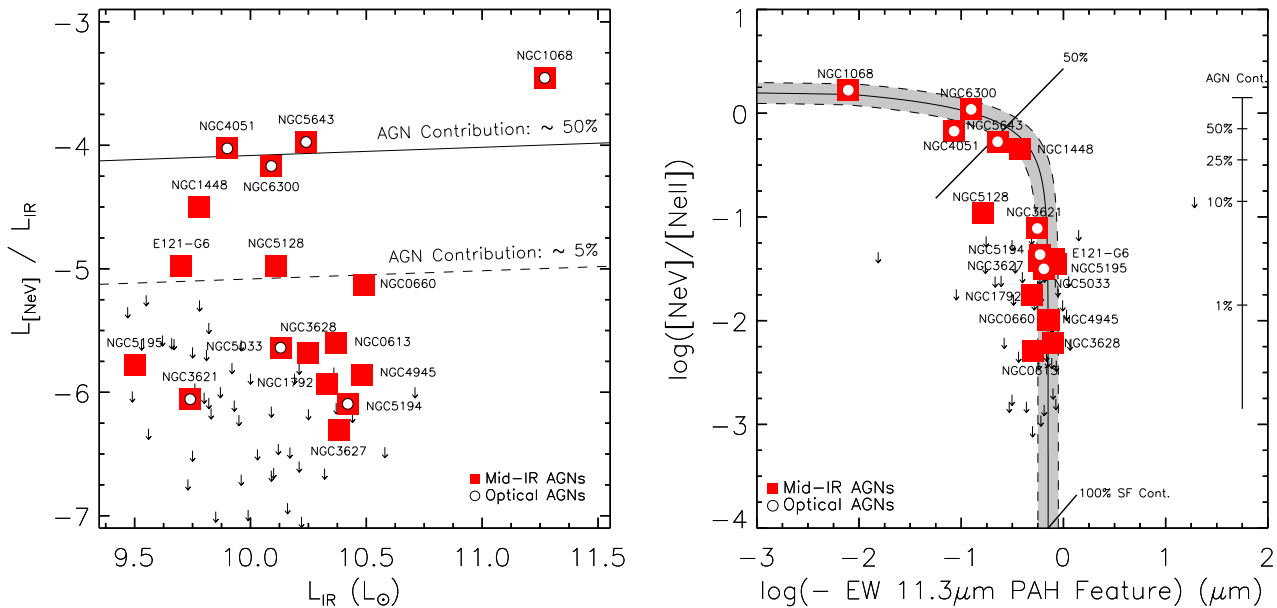


Figure 6. a; left): $[\text{NeV}] \lambda 14.32 \mu\text{m}$ -IR luminosity ratio versus IR luminosity. Mid-IR identified AGNs (filled squares) and optically identified AGNs (open circles) are indicated. The solid and dashed lines show the expected luminosity ratio for a ≈ 50 percent and ≈ 5 percent AGN contribution to the IR emission, respectively; adapted from Satyapal et al. (2007). Both the optically identified and unidentified AGNs span a wide range of $[\text{NeV}]$ -IR luminosity ratios. However, clearly the *Spitzer*-IRS observations are comparatively less sensitive towards the detection of $[\text{NeV}] \lambda 14.32 \mu\text{m}$ emission in the lowest IR luminosity bin ($L_{\text{IR}} < 10^{10} L_{\odot}$), indicating that the overall AGN fraction given in Fig. 5 should be considered a lower limit. **b; right):** Flux ratio of the $[\text{NeV}] \lambda 14.32 \mu\text{m}$ and $[\text{NeII}] \lambda 12.82 \mu\text{m}$ emission lines versus equivalent width of the $11.3 \mu\text{m}$ PAH feature ($\text{EW}_{11.3, \text{PAH}}$). Both the $\text{EW}_{11.3, \text{PAH}}$ and the $[\text{NeV}]$ - $[\text{NeII}]$ flux ratio give relative measures of the AGN-starburst contribution. The vertical scale indicates the fraction of AGN activity for the $[\text{NeV}]$ - $[\text{NeII}]$ flux ratio (Sturm et al. 2002). A linear mixing model curve (solid line) and 0.1 dex errors (dashed) are shown: a 100% AGN is assumed to have $[\text{NeV}]/[\text{NeII}] \sim 1.4$, $\text{EW}_{11.3, \text{PAH}} \sim 0.008 \mu\text{m}$, while a 100% starburst is assumed to have $[\text{NeV}]/[\text{NeII}] \sim 0.001$, $\text{EW}_{11.3, \text{PAH}} \sim 0.7 \mu\text{m}$.

cally identified AGNs. However, since approximately half of the optically identified AGNs are also star-formation dominated, dilution from star-formation signatures is unlikely to be the dominant cause for the lack of optical AGN signatures in all of the optically unidentified AGNs. Indeed, as we show in §3.2.3 and §3.3, strong $\text{H}\beta$ emission produced by young stars is likely to be the primary reason for the lack of AGN optical signatures (i.e., a low $[\text{OIII}]-\text{H}\beta$ ratio) in only three of the optically unidentified AGNs.

3.2.3 Are optically unidentified AGNs heavily dust obscured?

The dominant reason for the lack of AGN optical signatures could be due to dust obscuration. A good measure of dust obscuration within a host galaxy is the so-called Balmer decrement (the $\text{H}\alpha/\text{H}\beta$ flux ratio; e.g., Ward et al. 1987). In Table 1 we show that both the optically identified and optically unidentified AGNs cover similar ranges in Balmer decrements, apparently indicating no difference in optical extinction between the two populations. However, many late-type galaxies are found to be very dust/gas rich, and for galaxies such as these, the Balmer decrement may be a poor measure for high-levels of extinction. For example, NGC 4945 is an optically unidentified AGN (optically

classified as an HII galaxy), and using analyses at near-IR wavelengths it is estimated to have a V-band extinction of $A_V \approx 6$ –20 magnitudes (Moorwood et al. 1996); however, the optical Balmer decrement of the galaxy would suggest that it is relatively unobscured ($A_V \approx 0$ mags). To remove this ambiguity of additional attenuation to the optical emission, we require a measure of dust-obscuration that is capable of probing greater optical depths than optical spectroscopy alone.

Here we estimate the extinction towards the AGNs using $[\text{OIV}] \lambda 25.89 \mu\text{m}$ at mid-IR wavelengths and $[\text{OIII}] \lambda 5007\text{\AA}$ at optical wavelengths.¹⁰ $[\text{OIV}] \lambda 25.89 \mu\text{m}$ has often been used as a relatively dust-obscuration independent indicator of the AGN luminosity (e.g., Genzel et al. 1998; D06), and we show in §3.4 that it is reliable for $[\text{NeV}]$ -identified AGNs; however, see §3.4 for caveats in using $[\text{OIV}] \lambda 25.89 \mu\text{m}$ to directly identify AGN activity. By contrast,

¹⁰ We note that it would also be useful to determine the amount of extinction using the $[\text{NeV}]$ emission lines at $14.32 \mu\text{m}$ and 3426\AA . Unfortunately, this is not currently possible due to the lack of available data at ultra-violet wavelengths for the majority of our sample. Also, this ratio is additionally dependent on temperature variations of the photoionised gas within the narrow line region of the AGN.

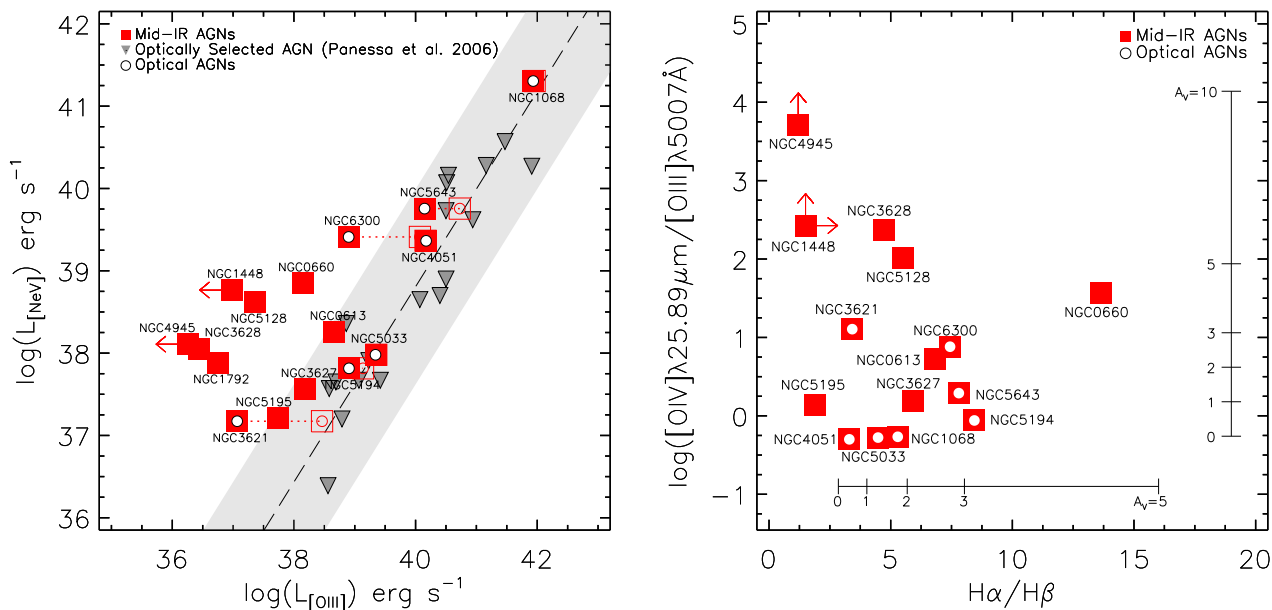


Figure 7. a; left $[\text{NeV}] \lambda 14.32 \mu\text{m}$ luminosity versus $[\text{OIII}] \lambda 5007\text{\AA}$ luminosity. Mid-IR identified AGNs (filled squares), optically identified AGNs (open circles), and optically selected AGNs from Panessa et al. (2006; filled triangles) are indicated. The $[\text{OIII}]$ luminosities for the Panessa et al. (2006) AGNs are corrected for extinction, and the *Spitzer*-IRS data is reduced and analysed following §2. The dashed line was obtained using a robust bi-sector linefit algorithm for the Panessa et al. (2006) sample (see Equation 1) and shows that the $[\text{NeV}] \lambda 14.32 \mu\text{m}$ luminosity provides a reliable measurement of the intrinsic luminosity of the AGN. The shaded region indicates the intrinsic scatter within the relation. The $[\text{NeV}]$ – $[\text{OIII}]$ luminosity ratios of the optically identified AGNs in our $D < 15$ Mpc sample are in good agreement with the $[\text{NeV}]$ – $[\text{OIII}]$ luminosity relationship when the $[\text{OIII}]$ luminosities are corrected for extinction using the Balmer decrement (dotted lines; see §3.2.3). Three of the optically unidentified AGNs (NGC 613, NGC 3627 and NGC 5195) are within the scatter of the relation indicating that these galaxies may not necessarily be extinguished in $[\text{OIII}]$ flux, but could have enhanced $H\beta$ flux from young stars as suggested in Fig 6b and 7b. **b; right** $[\text{OIV}] \lambda 25.89 \mu\text{m}$ and $[\text{OIII}] \lambda 5007\text{\AA}$ flux ratio versus Balmer decrement ($H\alpha/H\beta$ flux ratio). These ratios are indicators of the relative dust/gas extinction within the host galaxies, although the $[\text{OIV}]$ – $[\text{OIII}]$ flux ratio should be more sensitive towards high levels of extinction (see §3.2.3 and Diamond-Stanic et al. 2009); the solid lines indicate the relationship between the flux ratios and extinction in A_V . The symbols have the same meaning as in Fig. 6.

the optically detected $[\text{OIII}] \lambda 5007\text{\AA}$ emission lines produced in the narrow-line regions of AGNs can be subject to strong reddening by dust/gas, and therefore the $[\text{OIV}]$ – $[\text{OIII}]$ emission-line ratio should provide a good indicator for the presence of heavy obscuration. A similar approach using the $[\text{OIV}]$ – $[\text{OIII}]$ ratio has been taken by Diamond-Stanic et al. (2009) for assessing the obscuration in a sample of X-ray luminous AGNs. There could also be some dependence of the $[\text{OIV}]$ – $[\text{OIII}]$ ratio on the hardness of the radiation field (e.g., as measured using the $[\text{NeIII}]$ – $[\text{NeII}]$ ratio; Brandl et al. 2006); however, we find no strong dependence in our sample. We calibrate the extinction correction factor in A_V magnitudes by assuming $f_{[\text{OIII}]} \propto f_{[\text{OIV}]}^{1.8}$, as found for Seyfert 2 galaxies (e.g., Meléndez et al. 2008), combined with the expected dust-reddening at $\lambda \approx 5007\text{\AA}$ and $25.9 \mu\text{m}$ (e.g., Osterbrock & Ferland 2006). Although the $[\text{OIII}]$ emission-line constraints are typically obtained in a narrower slit than the $[\text{OIV}]$, since the majority of the $[\text{OIII}]$ and $[\text{OIV}]$ emission is likely to be produced close to the AGN (i.e., the ionising source), aperture effects are probably not significant.

In Fig. 7b we relate the two different measures of dust-extinction within the host galaxies obtained using the Balmer decrement and our $[\text{OIV}]$ – $[\text{OIII}]$ flux ratio estimate.

Similar levels of optical extinction are derived for the optically identified AGNs on the basis of both the Balmer decrement and the $[\text{OIV}]$ – $[\text{OIII}]$ flux ratios, implying moderate levels of dust obscuration ($A_V \sim 0$ –3 mags). However, by contrast, although optically unidentified AGNs have similar Balmer decrements to the optically identified AGNs, many have significantly higher $[\text{OIV}]$ – $[\text{OIII}]$ flux ratios. This suggests that the optically unidentified AGNs are so heavily extinguished at optical wavelengths that the Balmer decrement no longer provides a reliable estimate of the amount of obscuration, suggesting $A_V > 3$ mags. Indeed, on the basis of the $[\text{OIV}]$ – $[\text{OIII}]$ flux ratio for NGC 4945 we estimate that the AGN is obscured behind a screen of $A_V \sim 9$ magnitudes, which is in good agreement with the detailed constraints of Moorwood et al. (1996). Additionally, Alexander et al. (1999) find using near-IR spectroscopy $A_V \sim 7$ magnitudes for NGC 5128, which is again consistent with our extinction estimation derived from the $[\text{OIV}]$ – $[\text{OIII}]$ flux ratio ($A_V \sim 5$ magnitudes). We predict that if the $[\text{OIII}]$ emission was adjusted for an additional absorption within the narrow line region (NLR) as found by our diagnostic, these heavily extinguished optically unidentified AGNs would be moved into the Seyfert region of an optical BPT diagram. For example, assuming there is no further reddening to the $H\beta$ emission,

an additional NLR extinction of $A_V \sim 3$ is consistent with an increase by a factor of 6 in [OIII] flux (i.e., the correction required for NGC 5128 to be optically classified as a Seyfert galaxy; see Fig. 4).

In Fig. 7a, we show that three of the optically unidentified AGNs (NGC 0613, NGC 3627 and NGC 5195) are within the intrinsic scatter of the [OIII]-[NeV] relation (shaded region), and consequently do not appear to be deficient in [OIII] flux. Indeed, in Fig. 7b we find that these particular objects do not appear to be heavily extinguished at optical wavelengths ($A_V < 3$ mags). It is therefore likely that these are not classified as AGNs in optical surveys due to enhanced $H\beta$ flux from young stars, which lowers the [OIII]/ $H\beta$ flux ratio in a BPT diagram (see Fig. 4). This is in agreement with the AGN–star-formation ratios estimated for these objects with *Spitzer*-IRS; see Fig. 6b. However, it is clear from Fig. 7a,b that the majority of the optically unidentified AGNs are highly extinguished in [OIII] $\lambda 5007\text{\AA}$ flux.

3.3 First-order constraints on the source of the optical extinction

The obscuration towards some of the AGNs implied by Fig. 7a,b may be due to either a dusty torus (as predicted by the unified model for AGNs; e.g., Antonucci 1993) or extinction through the host galaxy (e.g., Malkan et al. 1998; Matt 2000). Here we can test the latter hypothesis by looking for evidence of host-galaxy extinction (i.e., a highly inclined galaxy or obscuring dust lanes) using available optical imaging; we defer exploration of the former hypothesis to Goulding et al. (in prep.) where we search for evidence of nuclear obscuration in our sample using sensitive X-ray observations. In Fig. 8 we compare optical images of the optically identified and unidentified AGNs. The optically identified AGNs in our sample are hosted by relatively face-on galaxies while, by contrast, many of the optically unidentified AGNs are hosted in either highly inclined galaxies or have dust lanes that obscure the central regions. Indeed, the four optically unidentified AGNs with the highest [OIV]–[OIII] flux ratios, which imply $A_V > 3$ mags, are all hosted by galaxies that are either highly inclined or have obscuring dust lanes; ESO121-G006 does not have good-quality optical spectroscopy, however, since it resides in a highly inclined host galaxy, it is likely to be an optically unidentified AGN with a high [OIV]–[OIII] flux ratio. Furthermore, three of the optically unidentified AGNs are found to be hosted in relatively face-on galaxies (NGC 0613, NGC 3627 and NGC 5195), similar to that of the optically identified AGNs, suggesting there is little extinction from the host galaxy towards these AGNs. This is consistent with our findings in the previous section that these galaxies do not appear to have heavily extinguished [OIII] emission (see Fig. 7a).

Our findings extend the analyses of Malkan et al. (1998), who found that dust lanes can dictate the observed optical AGN type, by now showing that the host galaxy can have a large effect on even the *identification* of AGN activity. We find that four ($\approx 40_{-19}^{+31}$ percent) of the ten optically unidentified AGNs reside in highly inclined galaxies, compared to ≈ 4 percent (Seyfert 1) and ≈ 7 percent (Seyfert 2) of the optically identified AGNs in Malkan et al. (1998), respectively. Four ($\approx 40_{-19}^{+31}$ percent) of the optically unidentified AGNs

also appear to have obscuring dust lanes, compared to ≈ 10 and ≈ 20 percent of the Seyfert 1 and Seyfert 2 galaxies in Malkan et al. (1998), respectively.¹¹ Whilst these findings are empirical and may be subject to small number statistics, there appears to be strong evidence to suggest that the non-identification of optical AGN signatures in the majority of these galaxies is due to extinction through the host galaxy, indicating that obscuration of the nucleus is not necessarily due to an obscuring torus. We also note that similar conclusions have been proposed for the non-identification of AGN signatures in $z \approx 0.5$ –1 X-ray identified AGNs (e.g., Rigby et al. 2006).

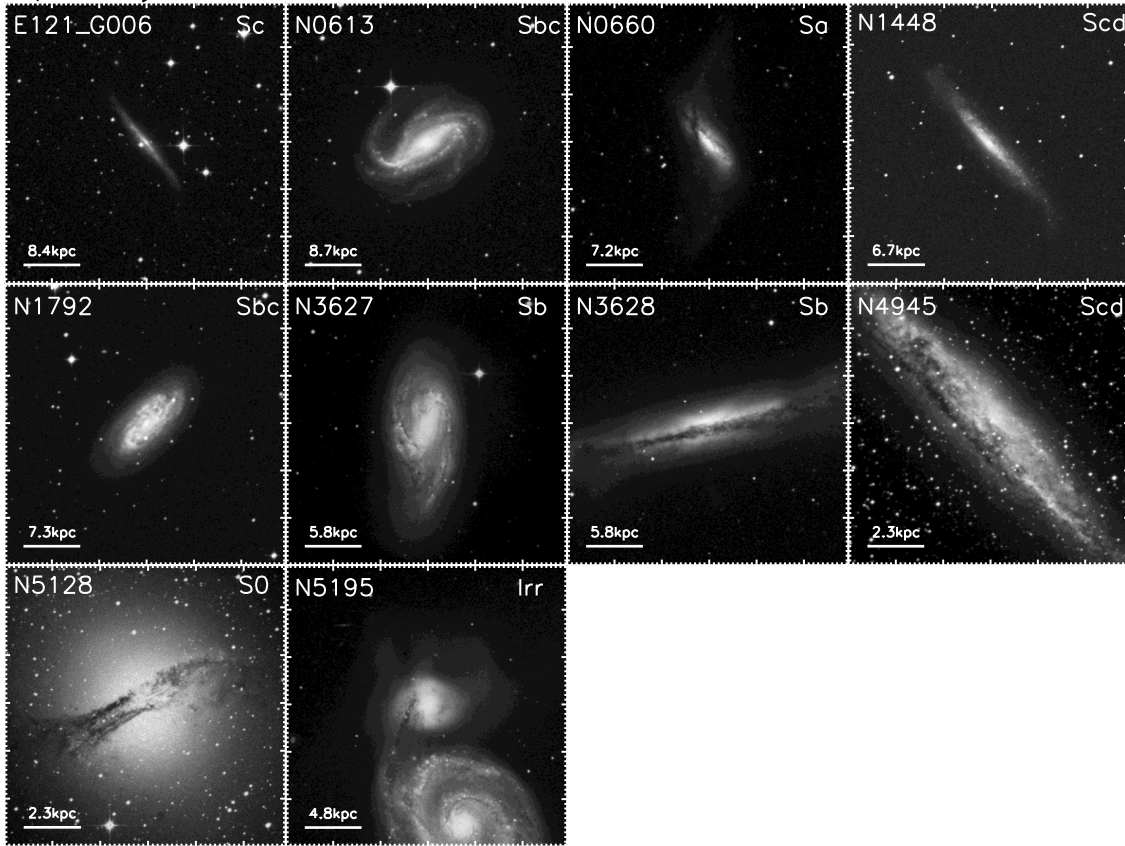
3.4 Can further AGNs be identified using other mid-IR emission-line diagnostics?

In our analyses thus far we have conservatively identified AGNs using the [NeV] $\lambda 14.32\ \mu\text{m}$ emission line. However, there may be further AGNs in our sample that can be identified using different mid-IR emission lines. Other studies have used the high-excitation emission line [NeV] $\lambda 24.32\ \mu\text{m}$, as well as intermediate-excitation emission lines such as [OIV] $\lambda 25.89\ \mu\text{m}$ (54.9 eV) and [NeIII] $\lambda 15.56\ \mu\text{m}$ (41.0 eV). To explore whether we can identify further AGNs in our sample, we investigate these other potential AGN indicators here.

[NeV] $\lambda 24.32\ \mu\text{m}$ has the same ionisation potential as [NeV] $\lambda 14.32\ \mu\text{m}$ but it has a higher critical electron density ($n_e \approx 5 \times 10^5$ versus $n_e \approx 5 \times 10^4\ \text{cm}^{-3}$; Sturm et al. 2002). [NeV] $\lambda 24.32\ \mu\text{m}$ is detected in 11 of the 64 galaxies in our sample, all of which are also detected at [NeV] $\lambda 14.32\ \mu\text{m}$. The smaller AGN identification fraction found using [NeV] $\lambda 24.32\ \mu\text{m}$ may be due to the lower relative sensitivity of data in the LH module in some cases. We also note that a large number of pixels around $\lambda \approx 24.3\ \mu\text{m}$ were damaged by solar flares early in the *Spitzer* mission, and are flagged by the *Spitzer* pre-processing pipeline as either damaged or unreliable (‘hot’ pixels). In our custom reduction pipeline we removed these pixels from the analysis and fitting routines to reduce the potential for spurious detections. For example, from analysis of the BCD images for NGC 3938 before and after cleaning using a custom version of IRSCLEAN, we find that the possible [NeV] $\lambda 24.32\ \mu\text{m}$ emission reported by S08 falls below our detection threshold of 3σ . Furthermore, an additional ‘hot’ pixel at $\lambda \sim 24.3594\ \mu\text{m}$ (in the observed frame) is not removed by default in IRSCLEAN due to the high incidence of adjacent cleaned pixels. During the reduction process, care must be taken to remove such pixels to ensure reliable detections. Additionally, we do not find any further AGNs in our $D < 15$ Mpc sample on the basis of the [NeV] $\lambda 24.32\ \mu\text{m}$ emission line and urge caution when identifying AGNs at low redshifts solely on the detection of weak [NeV] $\lambda 24.32\ \mu\text{m}$ with *Spitzer*-IRS observations. Certainly, at higher redshifts (i.e., where the observed [NeV] $\lambda 24.32\ \mu\text{m}$ emission is not affected by the spurious pixels at $\lambda \sim 24.35\ \mu\text{m}$) detections of weak [NeV] $\lambda 24.32\ \mu\text{m}$ without complimentary [NeV] $\lambda 14.32\ \mu\text{m}$ will be possible for systems with high levels of relative dust extinction; however, this is

¹¹ We note that high-resolution *HST* observations are required for the optically unidentified AGNs to provide a consistent comparison to Malkan et al. (1998).

Optically Unidentified AGNs



Optically Identified AGNs

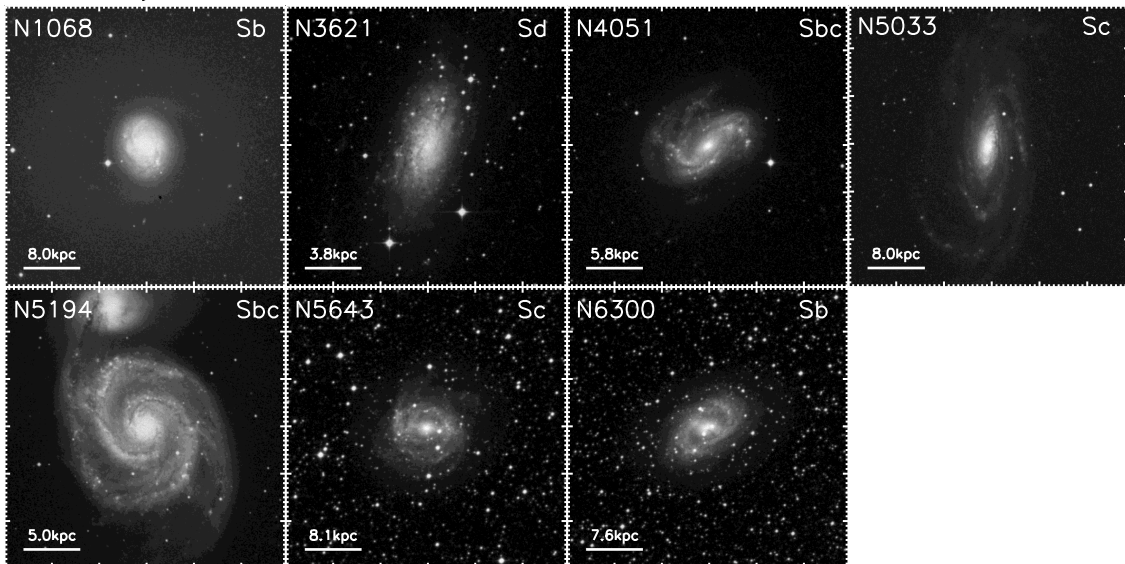


Figure 8. 10 × 10 arcmin ESO Digital Sky Survey images (combined *B* and *R* band) of the optically unidentified and optically identified AGNs. Optically unidentified AGNs are generally found to be hosted in either highly inclined galaxies (E121-G006, NGC 660, NGC 1448, NGC 3628 and NGC 4945) or galaxies with obscuring dust lanes (NGC 1792, NGC 3628, NGC 4945 and NGC 5128). This suggests that the lack of optical AGN signatures in these galaxies could be due to extinction through the host galaxy, indicating that obscuration of the nucleus is not necessarily due to an obscuring torus. Three of the optically unidentified AGNs (NGC 613, NGC 3627 and NGC 5195) appear to be hosted in relatively face-on galaxies; we suggest that the AGN optical signatures are diluted in these galaxies due to strong star-formation activity (see §3.2.2 & §3.2.3).

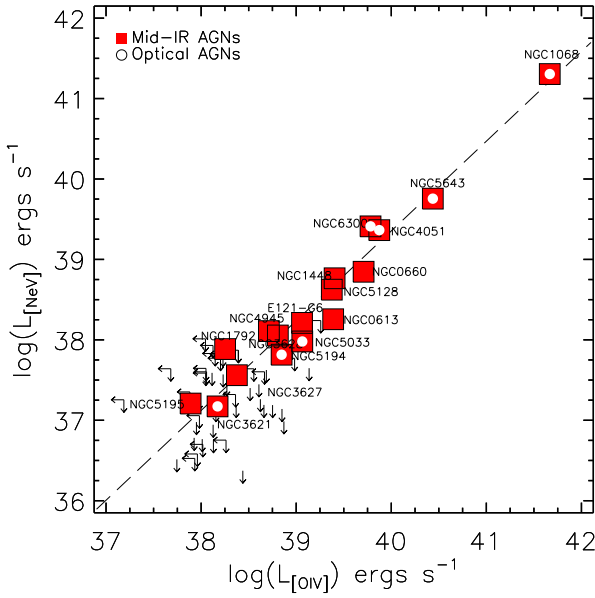


Figure 9. [NeV] $\lambda 14.32 \mu\text{m}$ luminosity versus [OIV] $\lambda 25.89 \mu\text{m}$ luminosity. The dashed line was obtained using a robust bi-sector linefit algorithm and indicates that for [NeV]–detected objects, [OIV] $\lambda 25.89 \mu\text{m}$ provides a good proxy for the intrinsic luminosity of the AGN (see Equation 2) for those galaxies with $10^{39} < L_{[\text{OIV}]} < 10^{42} \text{ erg s}^{-1}$. The symbols have the same meaning as in Fig. 6.

likely to be rare as $A_{14.32}/A_{24.32} \sim 1.03$ (Chiar & Tielens 2006).

[OIV] $\lambda 25.89 \mu\text{m}$ is often attributed to AGN activity. However, since it is an intermediate excitation emission line it can also be detected in galaxies experiencing heightened starburst activity (D06). [OIV] $\lambda 25.89 \mu\text{m}$ is detected in 41 of the 64 galaxies in our sample, including all of the 17 AGNs identified using [NeV]. For the mid-IR identified AGNs, we find that [OIV] $\lambda 25.89 \mu\text{m}$ and [NeV] $\lambda 14.32 \mu\text{m}$ emission are well correlated, suggesting that [OIV] $\lambda 25.89 \mu\text{m}$ is a good proxy for the intrinsic AGN luminosity in [NeV]–identified AGNs; see Fig. 9. The regressional fit is characterised by the equation given below, with a spread in the data of only 0.24 dex (see also Footnote 9). We highlight the caveat that this relation may only hold for the emission-line and IR luminosity range explored here. To rigorously assess the validity of this relation for all galaxies a further study probing a large luminosity range must be undertaken, which is beyond the scope of these analyses presented here.

$$\log[\text{NeV}] = (1.09 \pm 0.06) \log[\text{OIV}] - (4.34 \pm 2.53) \quad (2)$$

Our finding of a tight relationship between [OIV] $\lambda 25.89 \mu\text{m}$ and [NeV] $\lambda 14.32 \mu\text{m}$ suggests that any AGN activity with bright [NeV] $\lambda 14.32 \mu\text{m}$ emission should also have bright [OIV] $\lambda 25.89 \mu\text{m}$ emission. Contrary to this, S08 identified two AGNs (NGC 4321 and NGC 4536) using [NeV] $\lambda 14.32 \mu\text{m}$ that had undetected [OIV] $\lambda 25.89 \mu\text{m}$ emission. NGC 4536 is present in our sample but we do not identify [NeV] $\lambda 14.32 \mu\text{m}$ using our conservative reduction and analysis techniques. Four of the galaxies (IC2056;

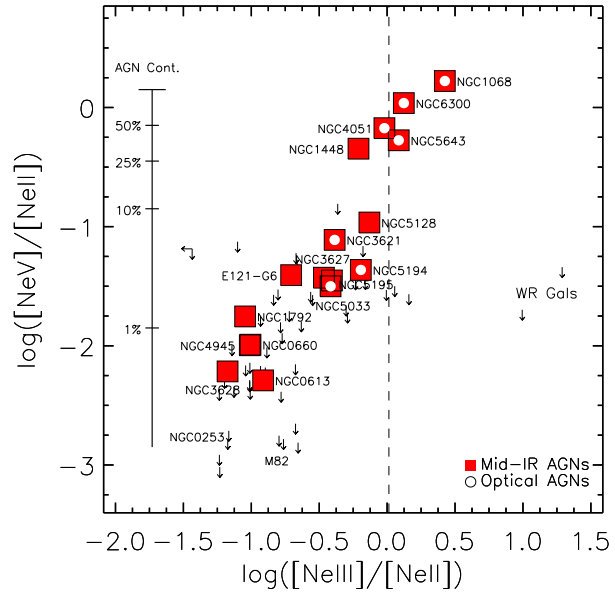


Figure 10. Logarithm of the ratio of the fluxes of [NeIII] $\lambda 15.51 \mu\text{m}$ and [NeII] $\lambda 12.82 \mu\text{m}$ emission lines are plotted against the logarithm of the ratio of the fluxes of [NeV] $\lambda 14.32 \mu\text{m}$ and [NeII] $\lambda 12.82 \mu\text{m}$ emission lines. The dashed line represents the demarcation for Seyfert 2 galaxies given in Meléndez et al. (2008). Those AGNs which dominate the luminosity output of the galaxy have preferentially higher [NeIII]/[NeII] ratios, and appears to be a good proxy for AGN activity in these cases. By contrast, lower luminosity AGNs exhibit similar ratios to that of star-forming galaxies. Wolf-Rayet galaxies introduce a further caveat to use of the [NeIII]/[NeII] ratio to indicate AGN activity, $([\text{NeIII}]/[\text{NeII}])_{\text{AGN}} \sim ([\text{NeIII}]/[\text{NeII}])_{\text{WR}}$. The symbols have the same meaning as in Fig. 6.

NGC 3175; NGC 3184; NGC 3368) in our sample with [OIV] $\lambda 25.89 \mu\text{m}$ detections lie above the regressional fit in Fig. 9 and more sensitive mid-IR spectroscopy may identify AGN activity with [NeV] $\lambda 14.32 \mu\text{m}$ in these systems. A further 20 galaxies undetected in [NeV] $\lambda 14.32 \mu\text{m}$ lie below the regressional fit and, therefore, unless AGNs can have weak [NeV] $\lambda 14.32 \mu\text{m}$ and bright [OIV] $\lambda 25.89 \mu\text{m}$ emission, these do not appear to host AGN activity. However, we note that the 13 galaxies in our sample that are undetected in both [OIV] $\lambda 25.89 \mu\text{m}$ and [NeV] $\lambda 14.32 \mu\text{m}$ may host AGN activity substantially below our detection limits. Furthermore, for galaxies with $L_{[\text{OIV}]} < 10^{39} \text{ erg s}^{-1}$, the source of the [OIV] emission becomes uncertain as a non-negligible fraction may be produced by star-formation (e.g., the starburst-AGN, NGC 4945). Therefore, the [OIV] emission may not be a strong tracer of the intrinsic luminosity of the AGN (i.e., the [NeV] luminosity) for galaxies with $L_{[\text{OIV}]} \ll 10^{39} \text{ erg s}^{-1}$. Further probes of the AGN luminosity (e.g., hard X-ray luminosities) are required to test this further and we defer this analysis to Goulding et al. (in prep.).

[NeIII] $\lambda 15.56 \mu\text{m}$ is also an intermediate excitation emission line and could be produced by AGN or star-formation activity. Previous surveys (e.g., Farrah et al. 2007; Groves et al. 2008; Meléndez et al. 2008) have selected potential AGNs on the basis of high [NeIII]–[NeII] flux ratios

([NeIII]/[NeII] > 1.03; Meléndez et al. 2008). In Fig. 10 we show that while this diagnostic identifies many of the AGN-dominated systems in our sample, it does not find all of the AGNs. The production of [NeIII] appears to be complex and may have strong dependences on star-formation, gas density, temperature, metallicity and AGN activity (Brandl et al. 2006); for example, there is a similar range of [NeIII]–[NeII] ratios for both the optically unidentified AGNs and the galaxies without clear signatures of AGN activity. Furthermore, the two WR galaxies in our sample also have high [NeIII]–[NeII] flux ratios, suggesting that further criteria are required to unambiguously identify AGN activity. However, three of our galaxies not identified as AGNs (NGC 4490; NGC 4736; NGC 6744) have high [NeIII]–[NeII] flux ratios and may host AGN activity below our [NeV] λ 14.32 μ m sensitivity limit.

4 CONCLUSIONS

We have presented the initial results of a sensitive volume-limited *Spitzer*-IRS spectral survey of all (≈ 94 percent) bolometrically luminous ($L_{\text{IR}} \gtrsim 3 \times 10^9 L_{\odot}$) galaxies to $D < 15$ Mpc. We place direct constraints on the ubiquity of AGN activity in the local universe. Our main findings are the following:

(1) By conservatively assuming that the detection of the high-excitation [NeV] λ 14.32 μ m emission line indicates AGN activity, we identified AGNs in 17 of the 64 galaxies in our sample. This corresponds to an AGN fraction of $\approx 27_{-6}^{+8}$ percent, a factor $\gtrsim 2$ greater than found using optical spectroscopy alone; further AGNs are likely to be identified below our [NeV] λ 14.32 μ m sensitivity limit. The large AGN fraction indicates a tighter connection between AGN activity and IR luminosity for galaxies in the local Universe than previously found, potentially indicating a close association between AGN activity and star formation.

(2) We explored whether the absence of optical AGN signatures in the optically unidentified AGNs is due to either an intrinsically low-luminosity AGN or dilution from star formation. We found that the optically unidentified AGNs are typically characterised as star-formation dominated galaxies hosting modest-luminosity AGNs ($L_{[\text{NeV}]} \approx 10^{37} - 10^{39} \text{ erg s}^{-1}$). However, since about half of the optically identified AGNs also have these properties, it seems unlikely that the dominant reason for the absence of optical AGN signatures is due to either an intrinsically low-luminosity AGN or overwhelming star-formation activity. Indeed, we find that only three of the optically unidentified AGNs may have enhanced $H\beta$ emission from young stars which could dilute the optical AGN signatures. We also showed that the absence of optical AGN signatures is not due to low-sensitivity optical data. See §3.2.1, §3.2.2, & §3.2.3.

(3) We explored whether the absence of optical AGN signatures in the optically unidentified AGNs is due to optical extinction. We found that the optically unidentified AGNs typically have larger [OIV] λ 25.89 μ m–[OIII] λ 5007Å flux ratios than the optically identified AGNs, indeed suggesting that their emission is typically heavily extinguished at optical wavelengths ($A_V \approx 3-9$ mags). Examination of optical images revealed that seven of the optically unidentified AGNs are hosted in highly inclined galaxies or galaxies with

dust lanes, indicating that obscuration of the AGN is not necessarily due to an obscuring torus. See §3.2.3 and §3.3.

We therefore conclude that optical spectroscopic surveys miss approximately half of the AGN population simply due to extinction through the host galaxy. Sensitive X-ray observations are required to determine what fraction of the optically unidentified AGNs are heavily obscured due to nuclear obscuration intrinsic to the AGN.

ACKNOWLEDGMENTS

We thank the referee for a considered and thorough report which has significantly improved the paper. We would also like to acknowledge useful conversations with A. Edge, J. Geach, B. Lehmer, M. Meléndez, J. Mullaney, and I. Smail. ADG is supported by the award of a Science & Technologies Facilities Council (STFC) studentship and DMA is funded by a Royal Society fellowship and the Leverhulme Trust. This research has made use of the NASA/IPAC Extragalactic Database (NED) and the NASA *Spitzer* Space Telescope which are operated by the Jet Propulsion Laboratory, California Institute of Technology, under contract with the National Aeronautics and Space Administration. We would like to acknowledge the use of the Sloan Digital Sky Survey (SDSS) data archive, funding provided from the Alfred P. Sloan Foundation.

REFERENCES

- Alexander D. M., Hough J. H., Young S., Bailey J. A., Heisler C. A., Lumsden S. L., Robinson A., 1999, MNRAS, 303, L17
- Antonucci R., 1993, ARA&A, 31, 473
- Armus L., Bernard-Salas J., Spoon H. W. W., Marshall J. A., Charmandaris V., et al. 2006, ApJ, 640, 204
- Baldwin J. A., Phillips M. M., Terlevich R., 1981, PASP, 93, 5
- Barth A. J., Strigari L. E., Bentz M. C., Greene J. E., Ho L. C., 2009, ApJ, 690, 1031
- Brandl B. R., Bernard-Salas J., Spoon H. W. W., Devost D., Sloan G. C., et al. 2006, ApJ, 653, 1129
- Chiar J. E., Tielens A. G. G. M., 2006, ApJ, 637, 774
- Croom S. M., Smith R. J., Boyle B. J., Shanks T., Miller L., Outram P. J., Loaring N. S., 2004, MNRAS, 349, 1397
- Dale D. A., Smith J. D. T., Armus L., Buckalew B. A., Helou G., Kennicutt Jr. R. C., Moustakas J., Roussel H., et al. 2006, ApJ, 646, 161
- Dale D. A., Smith J. D. T., et al. 2009, ApJ, 693, 1821
- de Vaucouleurs G., de Vaucouleurs A., Corwin Jr. H. G., Buta R. J., Paturel G., Fouque P., 1991, Third Reference Catalogue of Bright Galaxies. Volume 1-3, XII, 2069 pp. 7 figs.. Springer-Verlag Berlin Heidelberg New York
- Desroches L.-B., Ho L. C., 2009, ApJ, 690, 267
- Diamond-Stanic A. M., Rieke G. H., Rigby J. R., 2009, ArXiv e-prints
- Draine B. T., 2003, ARA&A, 41, 241
- Fan X., Hennawi J. F., et al. 2004, AJ, 128, 515
- Farrah D., Bernard-Salas J., Spoon H. W. W., Soifer B. T., Armus L., Brandl B., Charmandaris V., Desai V., Higdon S., Devost D., Houck J., 2007, ApJ, 667, 149

- Ganda K., Falcón-Barroso J., Peletier R. F., Cappellari M., Emsellem E., McDermid R. M., de Zeeuw P. T., Carollo C. M., 2006, *MNRAS*, 367, 46
- Gebhardt K., Bender R., Bower G., Dressler A., Faber S. M., Filippenko A. V., Green R., Grillmair C., Ho L. C., Kormendy J., Lauer T. R., Magorrian J., Pinkney J., Richstone D., Tremaine S., 2000, *ApJ*, 539, L13
- Gehrels N., 1986, *ApJ*, 303, 336
- Genzel R., Lutz D., Sturm E., Egami E., Kunze D., Moorwood A. F. M., Rigopoulou D., Spoon H. W. W., Sternberg A., Tacconi-Garman L. E., Tacconi L., Thatte N., 1998, *ApJ*, 498, 579
- Greene J. E., Ho L. C., Barth A. J., 2008, *ApJ*, 688, 159
- Groves B., Nefs B., Brandl B., 2008, *MNRAS*, 391, L113
- Hasinger G., Miyaji T., Schmidt M., 2005, *A&A*, 441, 417
- Heckman T. M., Kauffmann G., Brinchmann J., Charlot S., Tremonti C., White S. D. M., 2004, *ApJ*, 613, 109
- Higdon S. J. U., Devost D., Higdon J. L., Brandl B. R., Houck J. R., Hall P., Barry D., Charmandaris V., Smith J. D. T., Sloan G. C., Green J., 2004, *PASP*, 116, 975
- Ho L. C., Feigelson E. D., et al. 2001, *ApJ*, 549, L51
- Ho L. C., Filippenko A. V., Sargent W. L. W., 1997a, *ApJS*, 112, 315
- Ho L. C., Filippenko A. V., Sargent W. L. W., 1997b, *ApJ*, 487, 568
- Houck J. R., Roellig T. L., et al. 2004, *ApJS*, 154, 18
- Iwasawa K., Koyama K., et al. 1993, *ApJ*, 409, 155
- Kauffmann G., Heckman T. M., White S. D. M., et al. 2003, *MNRAS*, 341, 33
- Kewley L. J., Dopita M. A., Sutherland R. S., Heisler C. A., Trevena J., 2001, *ApJ*, 556, 121
- Kewley L. J., Heisler C. A., Dopita M. A., Lumsden S., 2001, *ApJS*, 132, 37
- Kirhakos S. D., Steiner J. E., 1990, *AJ*, 99, 1722
- Knapp G. R., Guhathakurta P., Kim D.-W., Jura M. A., 1989, *ApJS*, 70, 329
- Kormendy J., Richstone D., 1995, *ARA&A*, 33, 581
- Laurent O., Mirabel I. F., Charmandaris V., Gallais P., Madden S. C., Sauvage M., Vigroux L., Cesarsky C., 2000, *A&A*, 359, 887
- Li A., Draine B. T., 2001, *ApJ*, 554, 778
- Lutz D., Sturm E., Genzel R., Spoon H. W. W., Moorwood A. F. M., Netzer H., Sternberg A., 2003, *A&A*, 409, 867
- Magorrian J., Tremaine S., Richstone D., Bender R., Bower G., Dressler A., Faber S. M., Gebhardt K., Green R., Grillmair C., Kormendy J., Lauer T., 1998, *AJ*, 115, 2285
- Maiolino R., Comastri A., Gilli R., Nagar N. M., Bianchi S., Böker T., Colbert E., Krabbe A., Marconi A., Matt G., Salvati M., 2003, *MNRAS*, 344, L59
- Malkan M. A., Gorjian V., Tam R., 1998, *ApJS*, 117, 25
- Martín-Hernández N. L., Schaerer D., Peeters E., Tielens A. G. G. M., Sauvage M., 2006, *A&A*, 455, 853
- Matt G., Fabian A. C., Guainazzi M., Iwasawa K., Bassani L., Malaguti G., 2000, *MNRAS*, 318, 173
- Meléndez M., Kraemer S. B., Armentrout B. K., Deo R. P., Crenshaw D. M., Schmitt H. R., Mushotzky R. F., Tueller J., Markwardt C. B., Winter L., 2008, *ApJ*, 682, 94
- Meléndez M., Kraemer S. B., Schmitt H. R., Crenshaw D. M., Deo R. P., Mushotzky R. F., Bruhweiler F. C., 2008, *ApJ*, 689, 95
- Moorwood A. F. M., van der Werf P. P., Kotilainen J. K., Marconi A., Oliva E., 1996, *A&A*, 308, L1+
- Mould J. R., Huchra J. P., et al. 2000, *ApJ*, 529, 786
- Moustakas J., Kennicutt Jr. R. C., 2006, *ApJS*, 164, 81
- Osterbrock D. E., Ferland G. J., 2006, *Astrophysics of gaseous nebulae and active galactic nuclei*. *Astrophysics of gaseous nebulae and active galactic nuclei*, 2nd. ed. by D.E. Osterbrock and G.J. Ferland. Sausalito, CA: University Science Books, 2006
- Panessa F., Bassani L., Cappi M., Dadina M., Barcons X., Carrera F. J., Ho L. C., Iwasawa K., 2006, *A&A*, 455, 173
- Peeters E., Spoon H. W. W., Tielens A. G. G. M., 2004, *ApJ*, 613, 986
- Richards G. T., Strauss M. A., et al. 2006, *AJ*, 131, 2766
- Rigby J. R., Rieke G. H., Donley J. L., Alonso-Herrero A., Pérez-González P. G., 2006, *ApJ*, 645, 115
- Rigopoulou D., Kunze D., Lutz D., Genzel R., Moorwood A. F. M., 2002, *A&A*, 389, 374
- Risaliti G., Maiolino R., Salvati M., 1999, *ApJ*, 522, 157
- Sanders D. B., Mazzarella J. M., Kim D.-C., Surace J. A., Soifer B. T., 2003, *AJ*, 126, 1607
- Sanders D. B., Mirabel I. F., 1996, *ARA&A*, 34, 749
- Satyapal S., Vega D., Dudik R. P., Abel N. P., Heckman T., 2008, *ApJ*, 677, 926
- Satyapal S., Vega D., Heckman T., O'Halloran B., Dudik R., 2007, *ApJ*, 663, L9
- Schaerer D., Stasińska G., 1999, *A&A*, 345, L17
- Smith J. D. T., Armus L., et al. 2007, *PASP*, 119, 1133
- Spoon H. W. W., Koornneef J., Moorwood A. F. M., Lutz D., Tielens A. G. G. M., 2000, *A&A*, 357, 898
- Sturm E., Lutz D., Verma A., Netzer H., Sternberg A., Moorwood A. F. M., Oliva E., Genzel R., 2002, *A&A*, 393, 821
- Terashima Y., Wilson A. S., 2004, *ApJ*, 601, 735
- Ueda Y., Akiyama M., Ohta K., Miyaji T., 2003, *ApJ*, 598, 886
- Veilleux S., Kim D.-C., Sanders D. B., 1999, *ApJ*, 522, 113
- Veilleux S., Kim D.-C., Sanders D. B., Mazzarella J. M., Soifer B. T., 1995, *ApJS*, 98, 171
- Veilleux S., Osterbrock D. E., 1987, *ApJS*, 63, 295
- Ward M. J., Geballe T., Smith M., Wade R., Williams P., 1987, *ApJ*, 316, 138
- Weedman D. W., Hao L., Higdon S. J. U., Devost D., Wu Y., Charmandaris V., Brandl B., Bass E., Houck J. R., 2005, *ApJ*, 633, 706
- Werner M. W., Roellig T. L., et al. 2004, *ApJS*, 154, 1

This paper has been typeset from a \TeX / \LaTeX file prepared by the author.

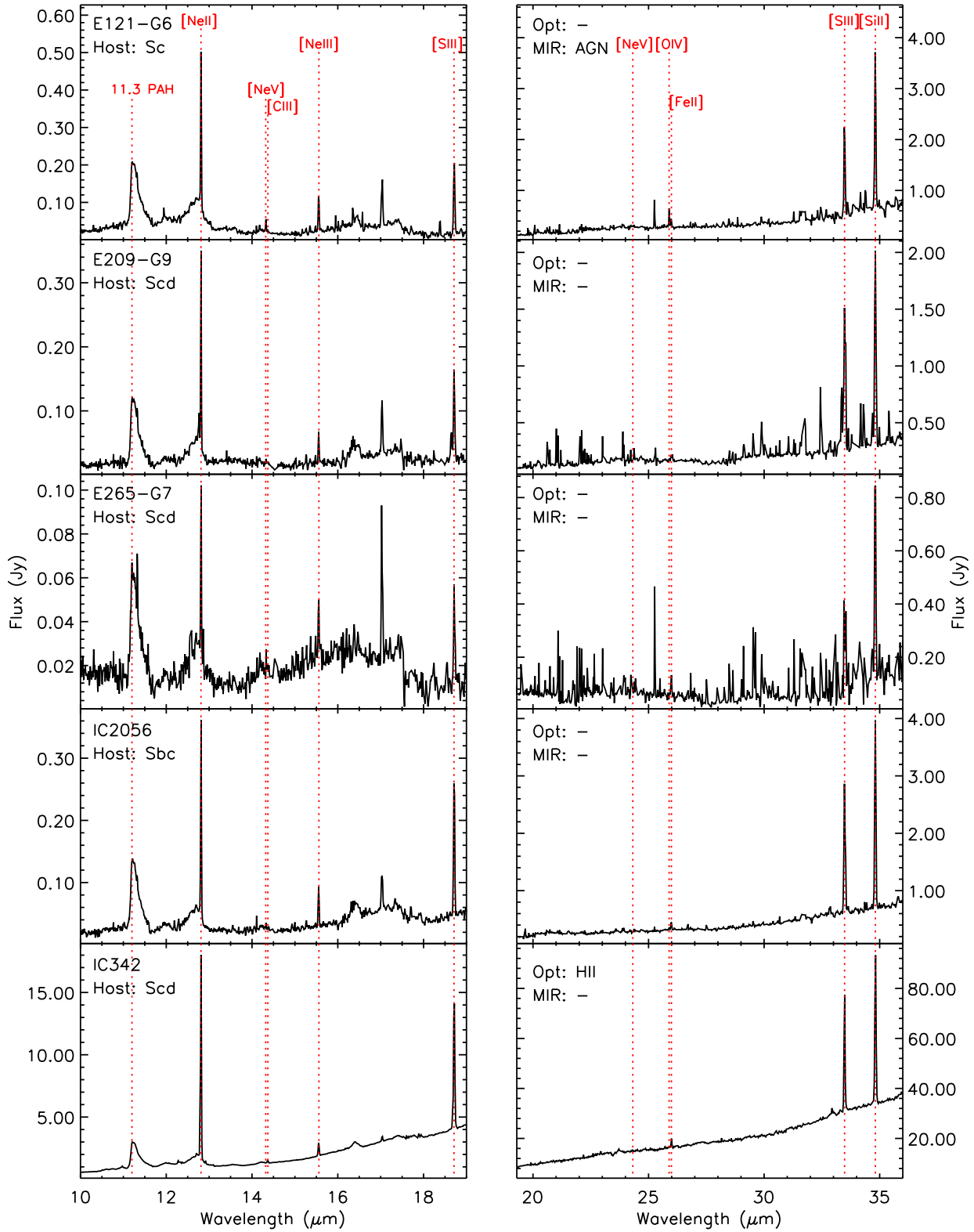


Figure 11. *Spitzer*-IRS high-resolution spectra for the SH and LH modules (left and right panels respectively) of all galaxies with *Spitzer*-IRS observations in our $D < 15$ Mpc IR-bright sample. The most prominent spectral features are labeled and indicated with dotted lines. The galaxy name, host-galaxy classification, optical spectral classification, and mid-IR classification are indicated.

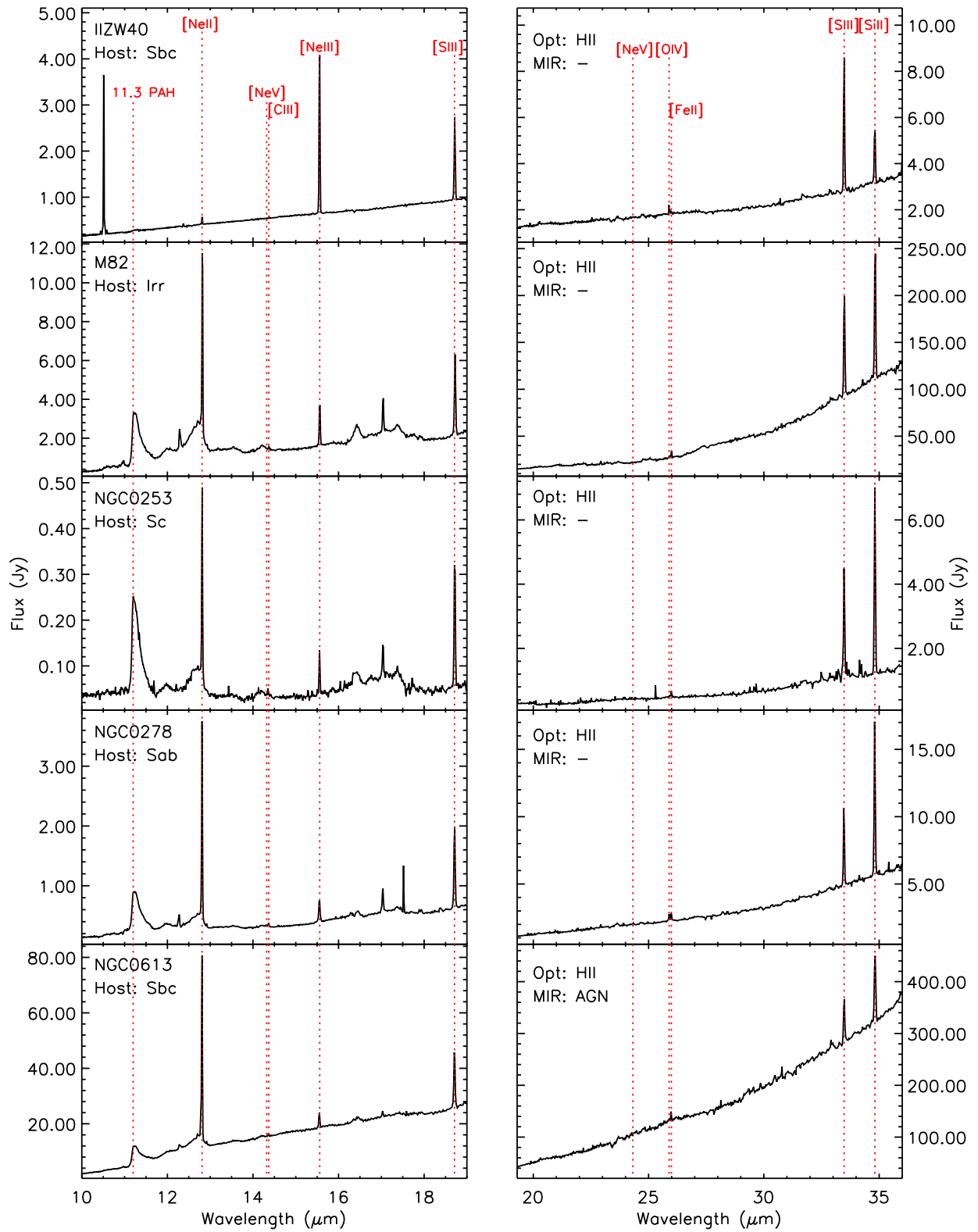


Figure 11 – continued

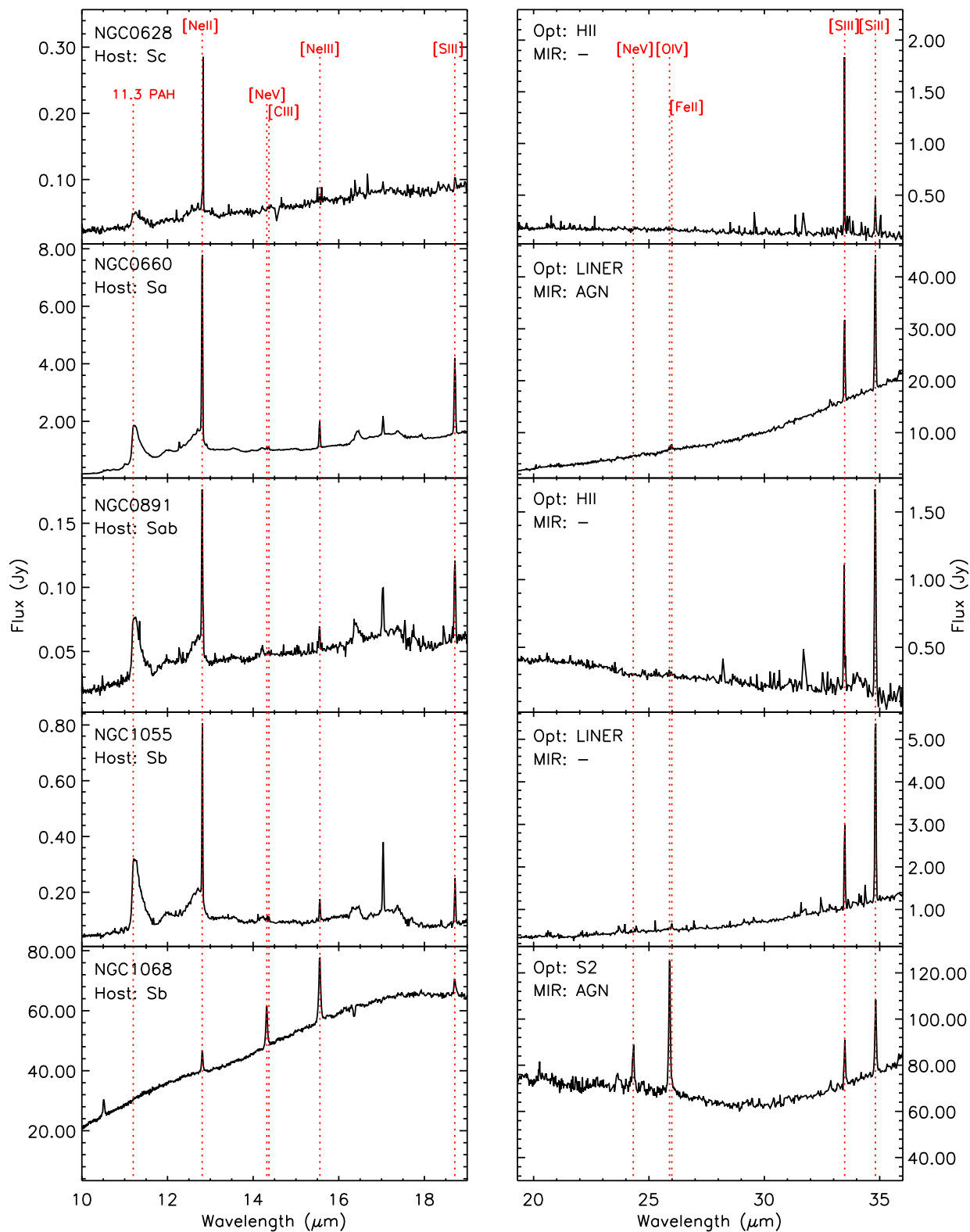


Figure 11 – continued

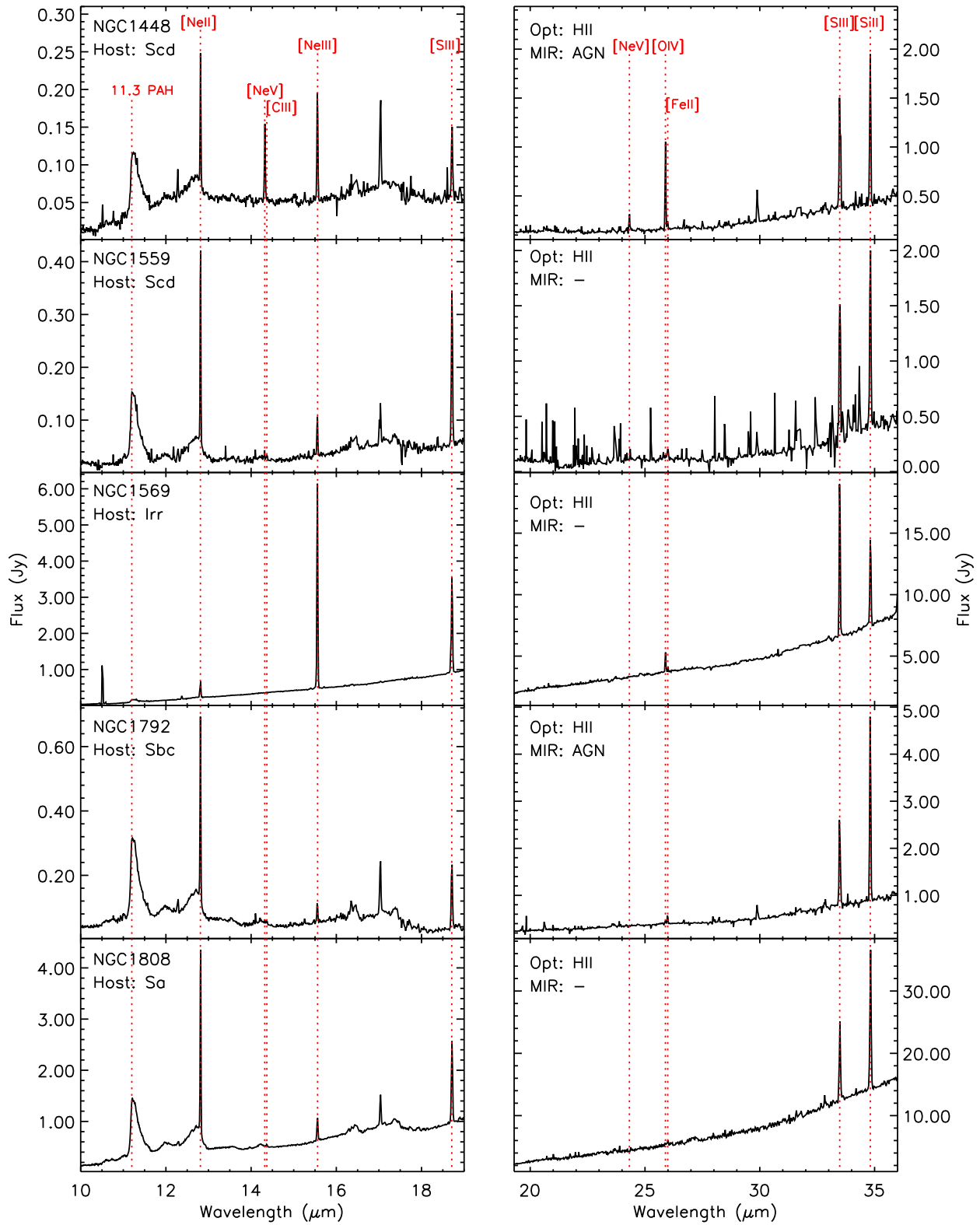


Figure 11 – *continued*

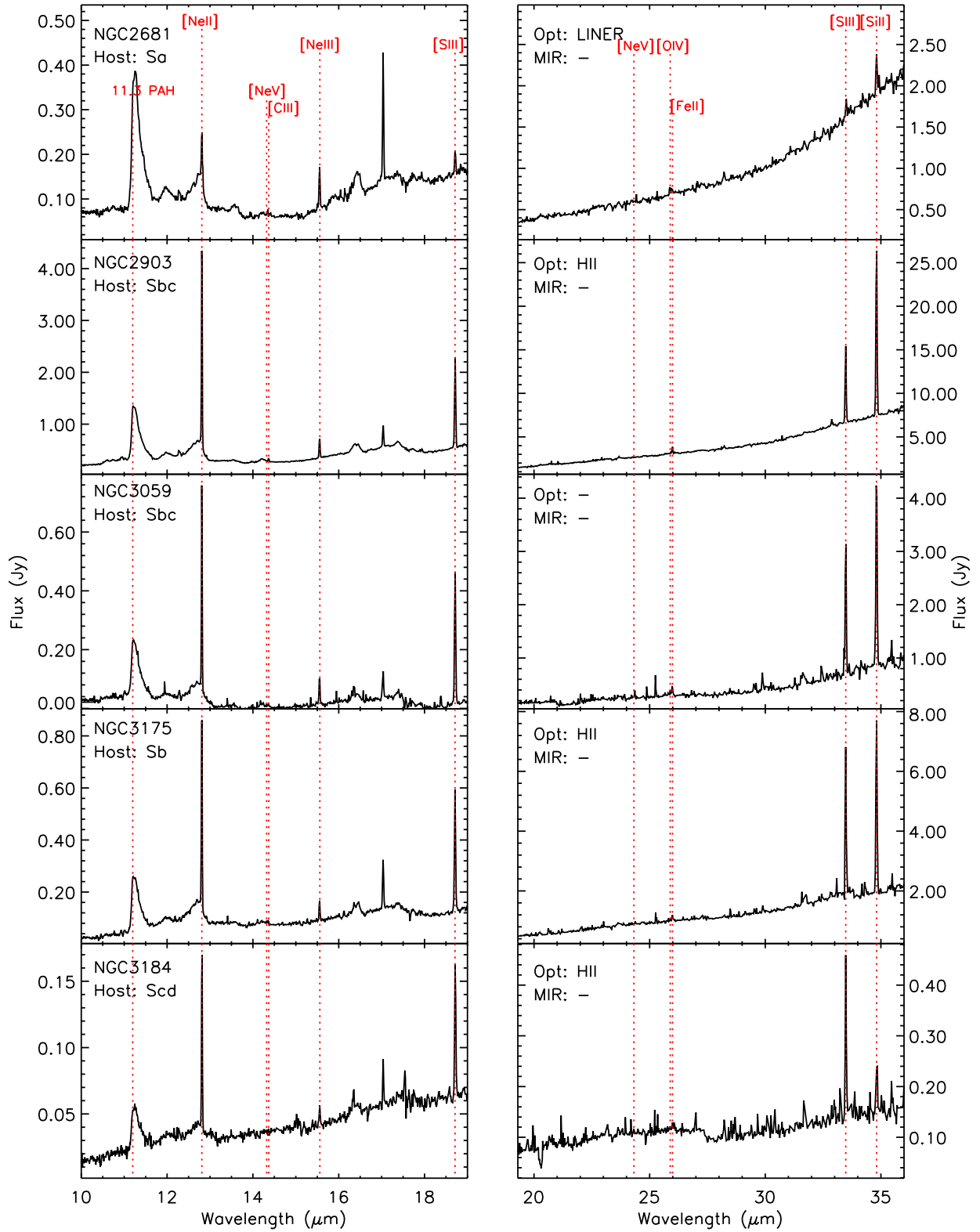


Figure 11 – continued

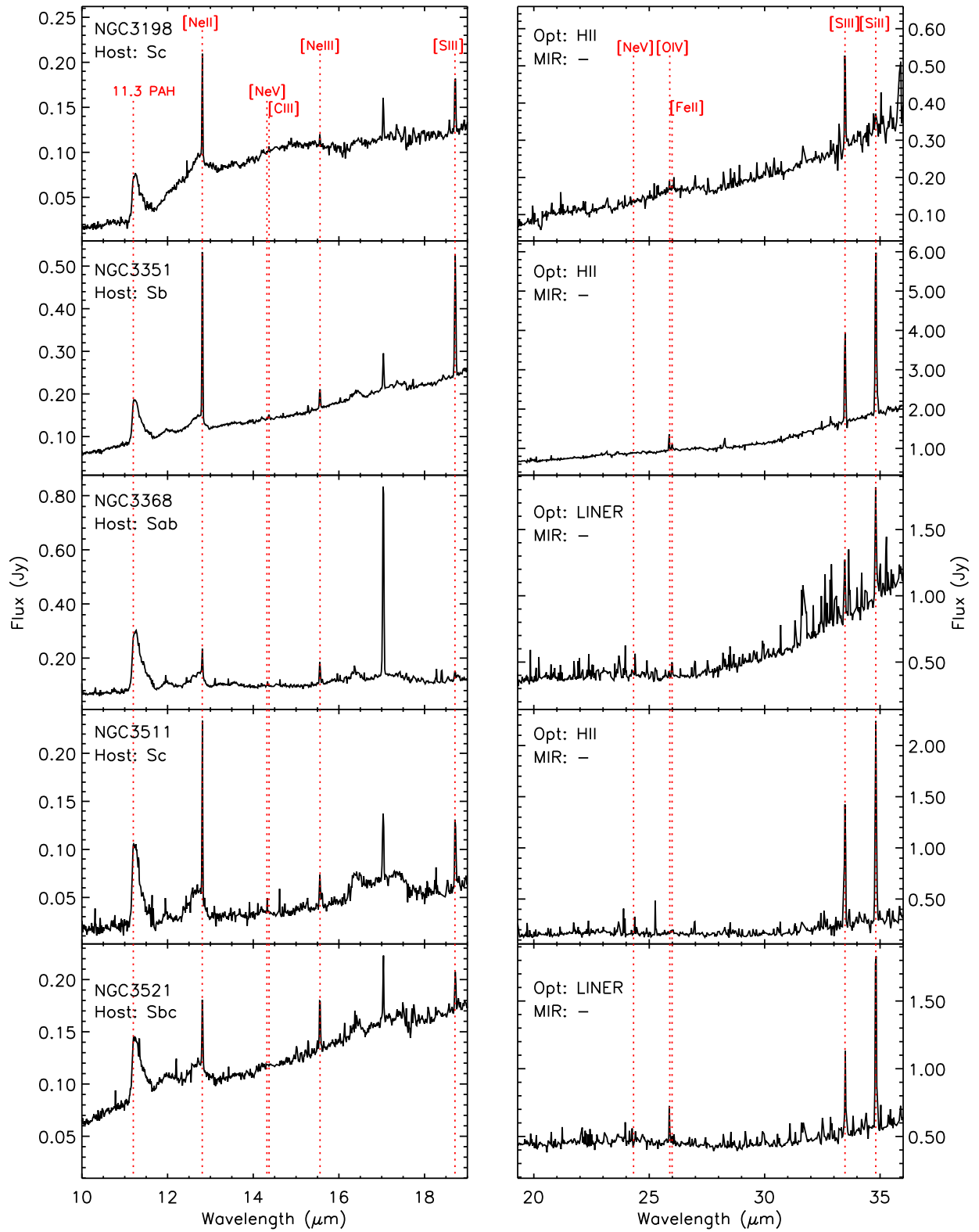


Figure 11 – *continued*

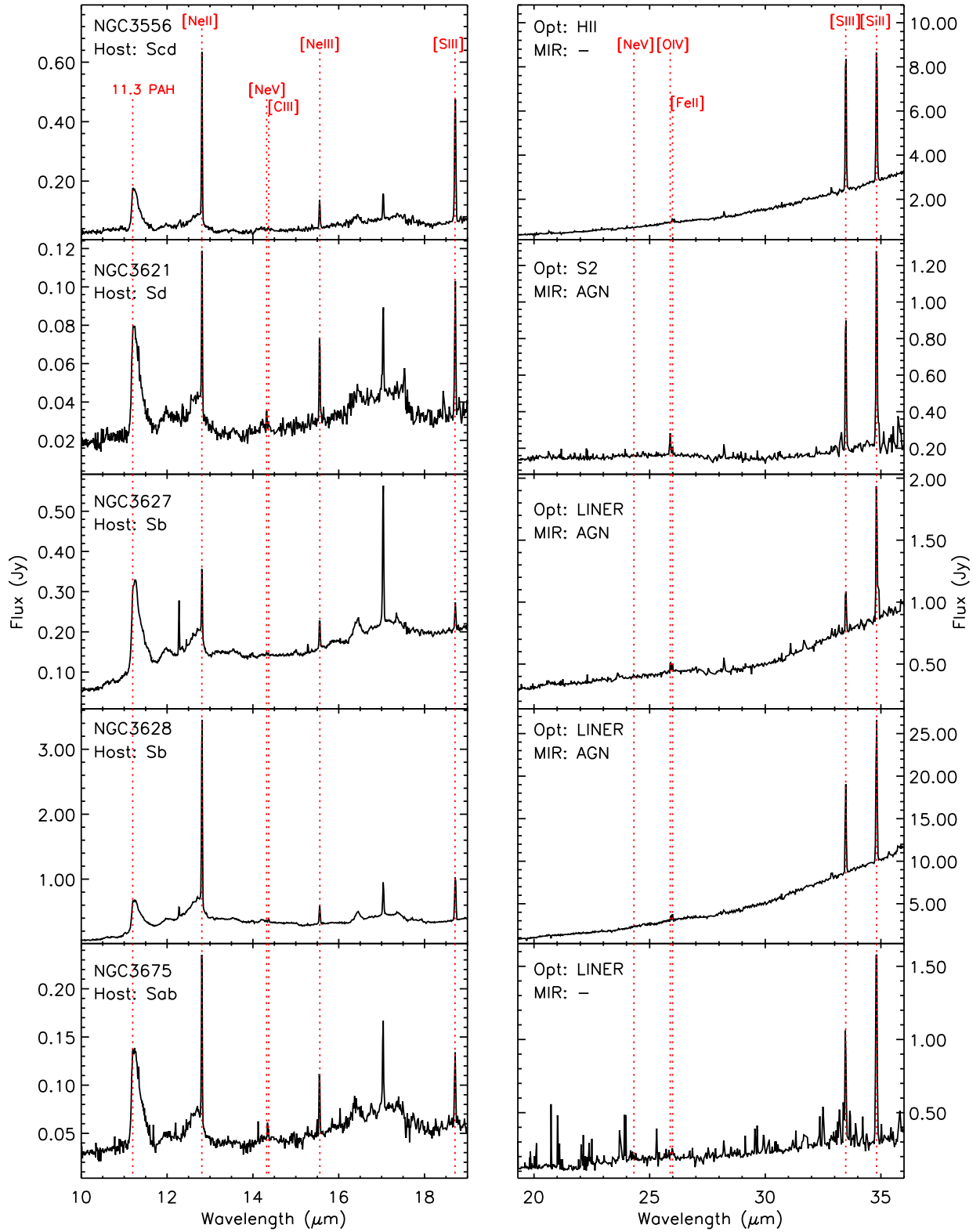


Figure 11 – continued

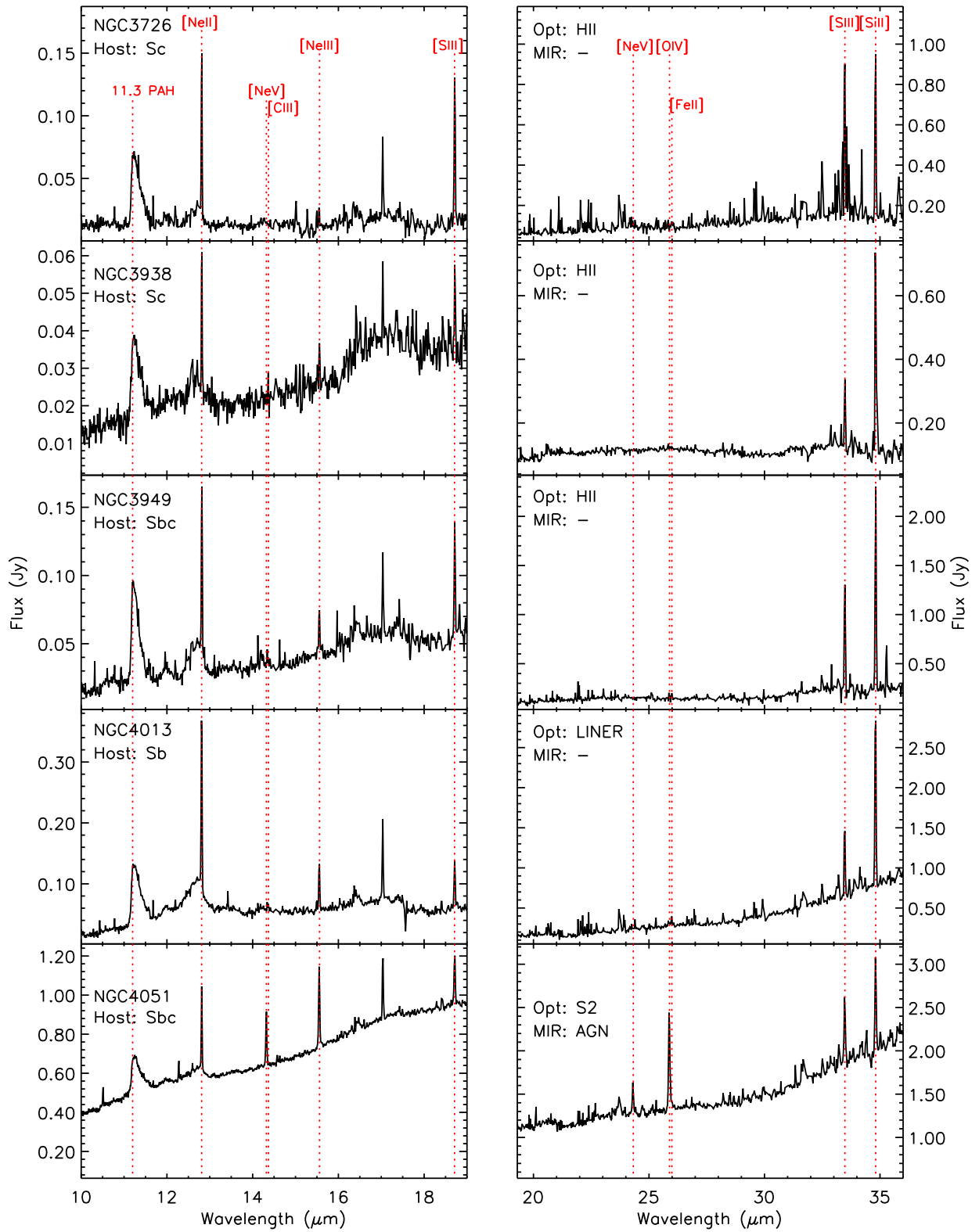


Figure 11 – *continued*

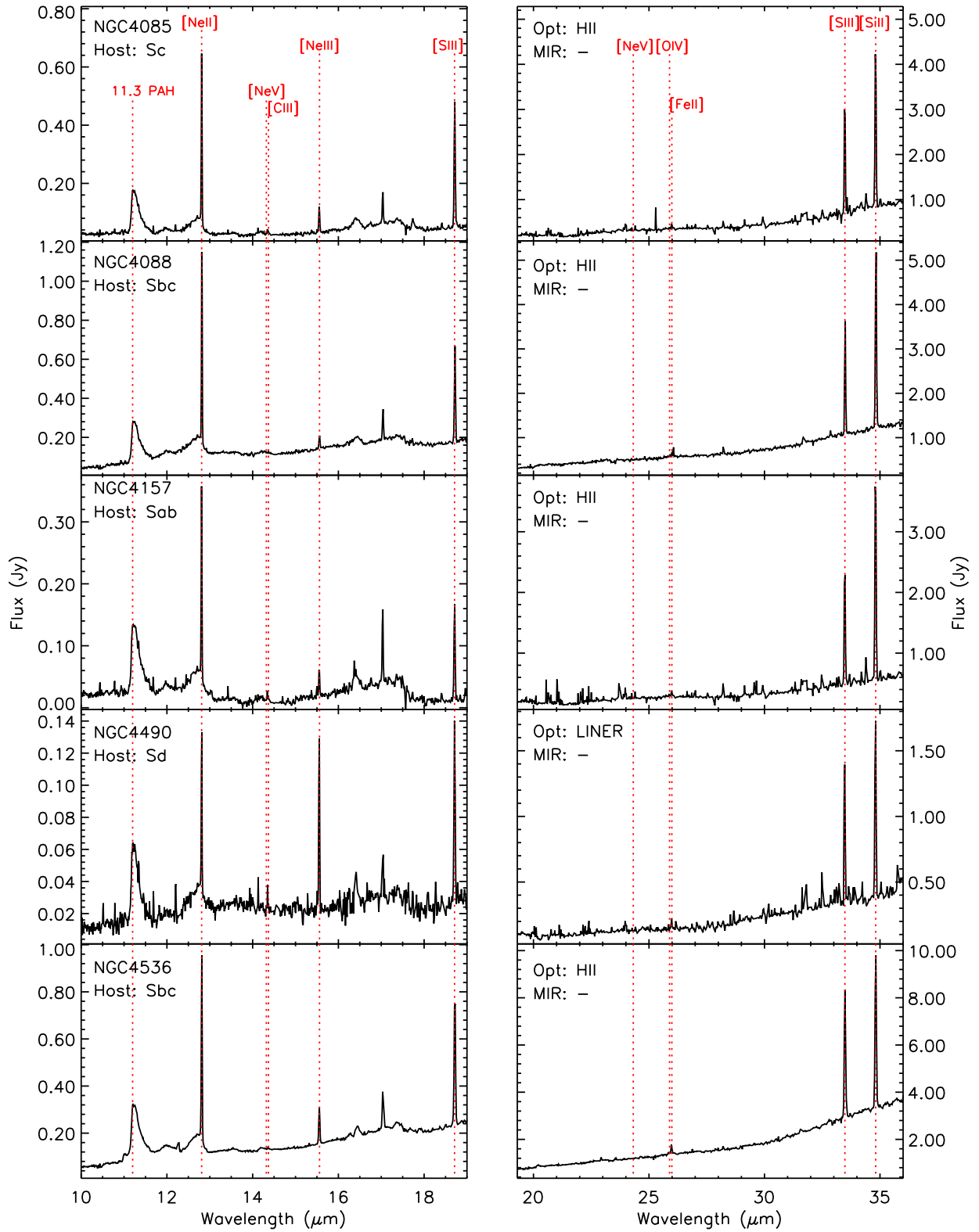


Figure 11 – continued

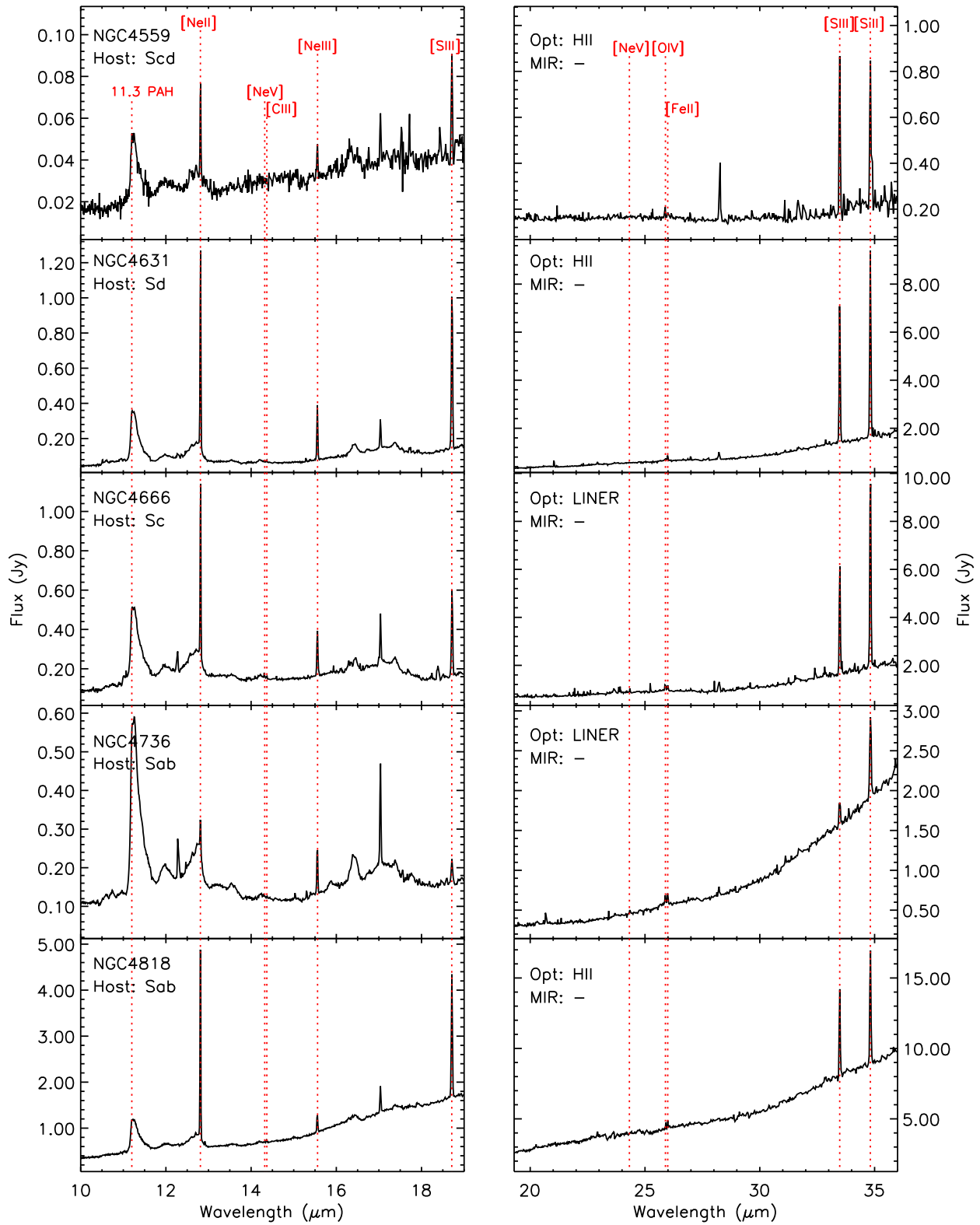


Figure 11 – *continued*

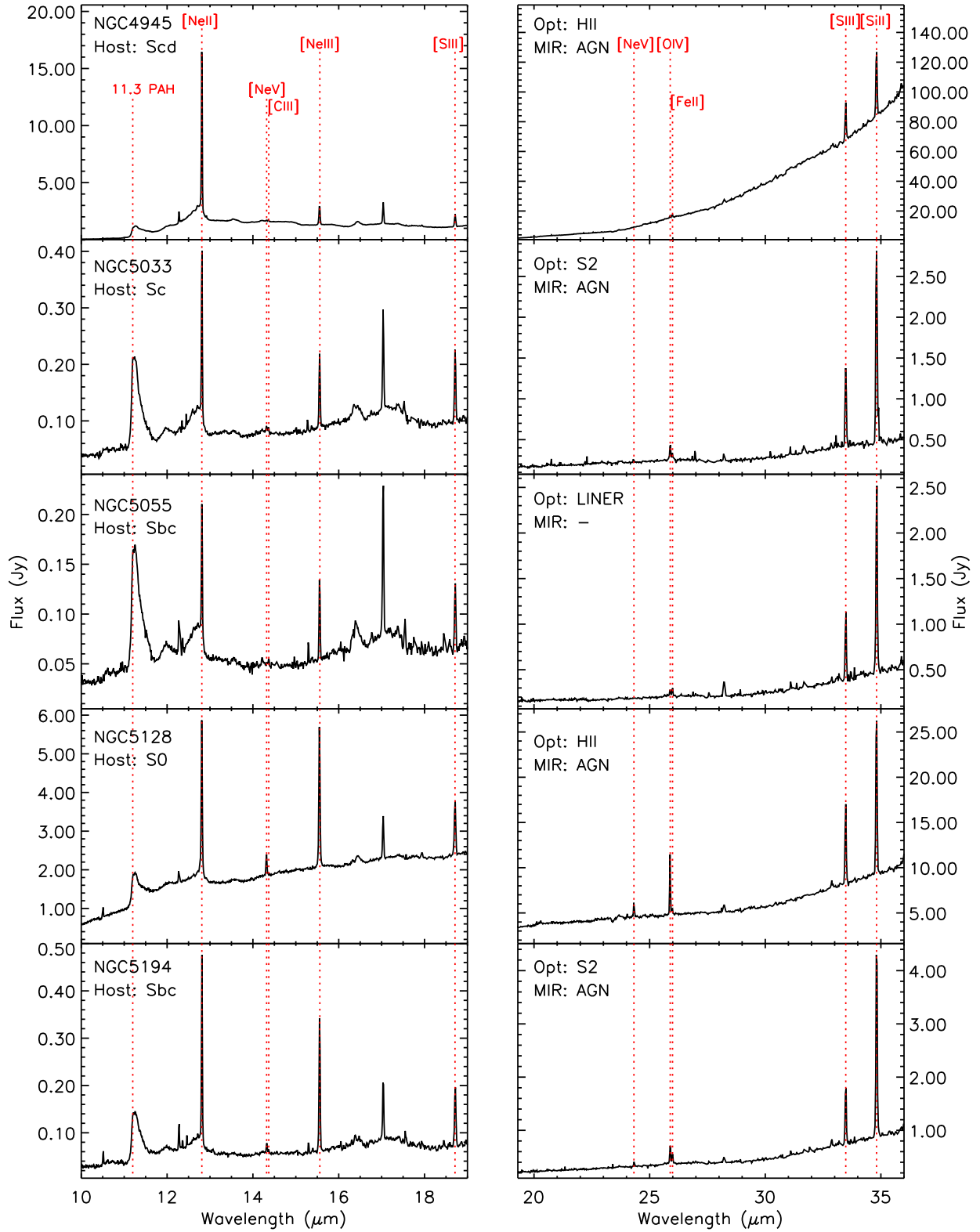


Figure 11 – continued

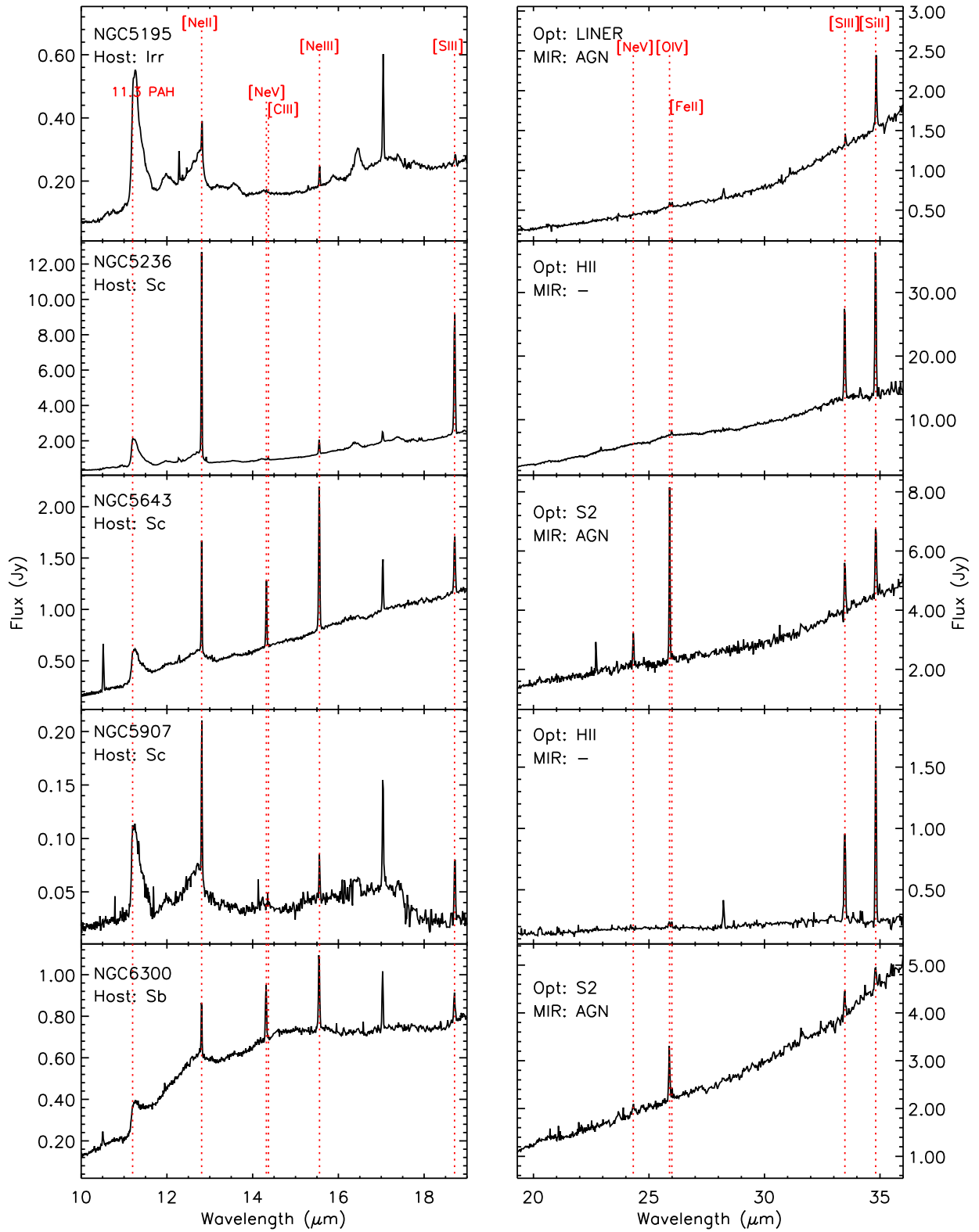


Figure 11 – *continued*

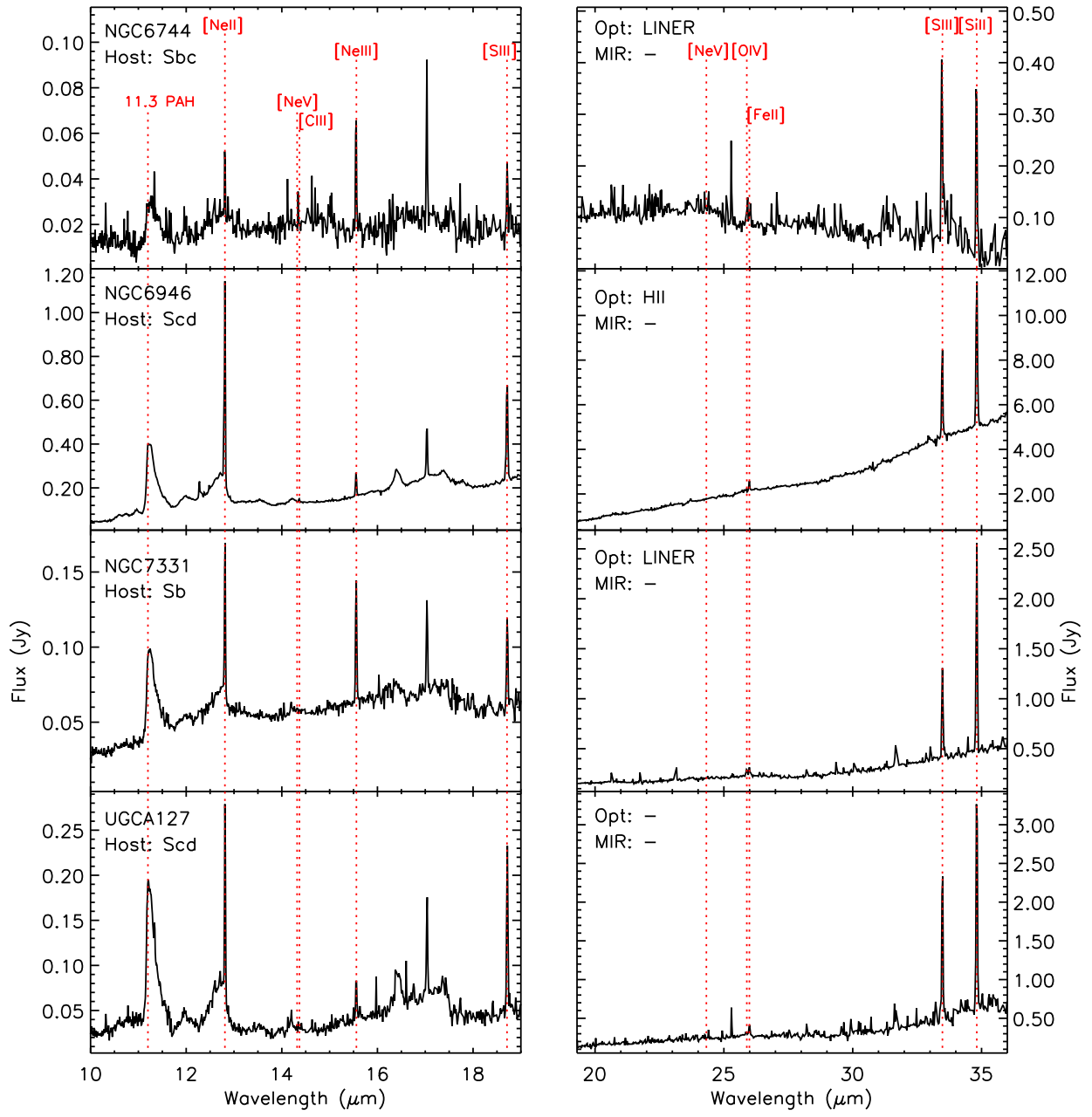


Figure 11 – continued